Near infrared signature of opaline silica at Mars-relevant pressure and temperature

Boris Chauviré, Maxime Pineau, Eric Quirico, Pierre Beck

Version of Record: https://www.sciencedirect.com/science/article/pii/S0012821X21004957
Manuscript_1433bb59267a5919aafb2bbcdfa060cc

Near infrared signature of opaline silica at Mars-relevant pressure and temperature

Boris Chauviré*[a], Maxime Pineau[b], Eric Quirico[c], Pierre Beck[c]

[a]*Univ. Grenoble Alpes, Univ. Savoie Mont Blanc, CNRS, IRD, IFSTTAR, ISTerre, 38000 Grenoble, France*
[b]*Université de Nantes, Université d'Angers, Laboratoire de Planétologie et Géodynamique, CNRS UMR 6112, BP 92208, 44322 Nantes, France*
[c]*Univ. Grenoble Alpes, CNRS, IPAG, 38000 Grenoble, France*
**Corresponding author: boris.chauvire@gmail.com, Université Grenoble Alpes, ISTerre, CS 40700, 38058*

GRENOBLE Cedex 9

Abstract

Opal is a mineral of great interest for tracing the aqueous Mars' history. Detection of opal on Mars is based on the near infrared (NIR) absorption bands related to the presence of water and hydroxyl. Because pressure and temperature can affect the amount and configuration of water in hydrated minerals, the associated absorption bands can be sensitive and vary according to the environmental conditions at the surface of Mars. In this study, the effects of Mars' relevant surface pressure and temperature on opal's NIR signature was investigated. By exposing opal samples to pressures varying between 1 and 8 mbar, and temperatures between -51.1 and -96.5°C, significant changes in opal samples' NIR features were observed. It was demonstrated that opal releases molecular water at low pressure, inducing changes on all NIR bands, as also observed in previous studies. However, such dehydration was not systematic, as it was noticed for only six out thirteen opal samples. When exposed to low temperature, water molecules in opal froze, inducing significant variation in shape and position of the bands at 5200 cm^{-1} and 7000 cm^{-1} (1.9 µm and 1.4 µm respectively). Low temperature experiments demonstrate that opal, and particularly opal-CT, can exhibit a water ice-like spectral signature. Such experimental data were compared with silica signature detected on Mars by CRISM and it was evident that martian opaline silica has a spectral signature specific of water ice, notably a shoulder near 5100 cm^{-1} (1.96 µm) and a wider 7000 cm^{-1} (1.4 µm) feature. We

show that opal can retain water under martian conditions, and that ancient water can be trapped following its precipitation.

Keywords: Opal, water, CRISM, low pressure, low temperature, ice

1. Introduction

Tracing the presence of liquid water, and its association with potential habitable environments during Mars' history, is an outstanding science goal and a major driver for Mars exploration. There is now clear evidence of the past presence of liquid water at the surface of Mars, based on geomorphological (e.g. Fassett and Head, 2008; Hauber et al., 2013) and mineralogical (e.g. Bibring et al., 2005; Carter et al., 2013a; Mustard et al., 2008) studies. The interaction of rocks with liquid water triggers the hydrolysis of anhydrous minerals, releasing silica in the altering fluids, and subsequently the precipitation of a variety of secondary hydrated minerals. Among all hydrated phases identified so far, hydrated silica has been detected through both orbit- and rover-based instruments (Milliken et al., 2008; Squyres et al., 2008) at many places across the planet (e.g. Carter et al., 2013a; Pan et al., 2021; Pineau et al., 2020; Sun and Milliken, 2018). This phase represents a promising target for astrobiological purposes, as opaline silica hosts the most ancient biological signatures on Earth (Djokic et al., 2017). In this respect, if well-preserved hydrothermal deposits were identified on Mars, they would be high priority targets for investigating evidence of past life (Des Marais and Walter, 2019; Teece et al., 2020). Importantly, the recent finding of a nymphal fossil, along with well-preserved organic material, in an opaline silica formed through recent continental weathering, has revealed that silica formed in weathering context may constitute a new source of ancient life fossils (Chauviré et al., 2020; Pan et al., 2021; Pineau et al., 2020).

The exact formation pathway of these opaline silica occurrences remains interpretative; however, it appears in a wide range of geological contexts, from sedimentary environments to hydrothermal systems. For instance, rovers surveying Mars surface have detected the presence of opaline silica; at Gusev crater, the rover Spirit (Mars Exploration Rover-A) reported silica-rich soils, interpreted as an evidence of hydrothermal activity, either formed by acid leaching or by direct precipitation (Ruff et al., 2020, 2011; Ruff and Farmer, 2016; Squyres et al.,

2008). Moreover, the *Curiosity* rover (Mars Science Laboratory, MSL) found silica-rich materials, identified as tridymite in a laminated mudstone (Morris et al., 2016), as well as diagenetic amorphous to crystalline silica in the Gale crater's stratigraphic sequence (Czarnecki et al., 2020; Frydenvang et al., 2017; Rampe et al., 2017; Rapin et al., 2018). Hydrated silica is also present on the landing site chosen for both the NASA rover *Perseverance* (Mars 2020 in Jezero crater; Pan et al., 2021; Tarnas et al., 2019) and the ESA rover *Rosalind Franklin* (ExoMars2022 in Oxia Planum ; Carter et al., 2012; Pan et al., 2021, 2019).

The ongoing or future rovers could provide sufficient information to distinguish the exact silica phases. Importantly, among opaline silica, which refers to a large family of silica phases, opal ($SiO_2.nH_2O$) represents the natural hydrated non-crystalline to poorly crystalline silica phases. Two main types of opal are usually differentiated: (1) opal-A, consisting of amorphous silica; and (2) opal-CT composed by tridymite nano-domains with variable proportion of non-crystalline domains. Opal-CT can be interpreted as a solid solution depending on the proportion of various domains (Elzea and Rice, 1996; Fröhlich, 2020; Jones and Segnit, 1971; Wilson, 2014). Opal types can easily be determined by either XRD or Raman spectroscopy (Curtis et al., 2019; Fritsch et al., 2012; Ostrooumov et al., 1999).

All opal varieties may contain water species (molecular water and OH groups; up to 15 % weight), entailing strong absorptions bands in the near infrared (NIR) region (Boboň et al., 2011; Chauviré et al., 2017; Langer and Flörke, 1974; Rice et al., 2013). In the 4500 cm^{-1} (2.2 µm) region, the combination of OH stretching and siloxane bending indicates the presence of silanols groups. By contrast, the combination of OH and H_2O modes in molecular water absorbs in the 5200 cm^{-1} (1.9 µm) region. Both bands are characterized by two main overlapping absorptions [at 4500 cm^{-1} (2.21 µm) and 4420 cm^{-1} (2.26 µm); 5250 cm^{-1} (1.91 µm) and 5100 cm^{-1} (1.96 µm)], with the higher energy component attributed to less H-bonded silanols or molecular water (Langer and Flörke, 1974). Similarly, the 7000 cm^{-1} (1.4 µm)

region exhibits two main components, due to a combination of OH stretching and bending in water molecules near 6850 cm^{-1} (1.46 µm) and OH stretching overtones near 7100 cm^{-1} (1.41 µm). In commercial silica gel, Christy (2010) identified the presence of isolated silanols by the band at 4579 cm^{-1} and 7316 cm^{-1} (2.18 µm and 1.37 µm), never seen in natural opal except after heating or low-pressure exposure (Boboň et al., 2011; Milliken et al., 2008; Rice et al., 2013).

Infrared signatures are the main criteria used to identify opaline silica by orbital instruments (e.g. Compact Reconnaissance Imaging Spectrometer for Mars – CRISM ; Milliken et al., 2008; Pineau et al., 2020; Sun and Milliken, 2018; Weitz et al., 2010). Previous studies had shown that these features may vary depending on the analytical conditions, specifically in terms of atmospheric pressure and temperature (Milliken et al., 2008; Sun, 2017; Sun and Milliken, 2018; Swayze et al., 2007; Thomas et al., 2020). Consequently, the use of laboratory opal spectra acquired in ambient terrestrial conditions for detection on Mars' surface should be made cautiously.

The effect of Mars-relevant pressure and temperature on opaline silica has been investigated by few studies (Poitras et al., 2018; Rice et al., 2013; Sun 2017; Sun and Milliken, 2018). At Mars' relevant temperatures, the silica phase containing water molecules should exhibit infrared features typical of ice, as observed in low temperature experiments (Poitras et al., 2018; Rice et al., 2013; Sun and Milliken, 2018; Thomas et al., 2020). In natural opal, the water freezing point is depressed (from -5°C to -47°C) due to the surficial interaction (Chauviré and Thomas, 2020; Thomas et al., 2020, 2013); this is a phase transition that occurs within the range of temperatures prevailing on Mars (Smith et al., 2017). The effect of Mars-like pressure was demonstrated to cause significant change in the opal's NIR strongest absorption bands, thus showing that molecular water is pumped out from the pores; on the other hand, effects of low temperature remain scarcely investigated.

In this study, we investigate the effect of typical martian pressures and temperatures on the NIR signature of a series of natural opal samples, and provide spectral proxies to facilitate their detection through infrared remote sensing. Transmission infrared spectra were collected on opaline silica chips, providing insights into compositional changes in bulk samples. We report on the water speciation and its evolution according to pressure and temperature conditions, and the associated spectral evolution in the near-infrared spectral range. The effects of different conditions are estimated in term of positions (apparent maximum, thus the local maximum independently of the position of the constitutive component) and ratio between components, i.e., parameters that can be easily compared with reflectance spectra. The application of these new spectral tracers to Mars NIR observations suggest that water is mostly present as water ice in opaline silica.

2. Materials and Methods

2.1. Opal Samples

For this study, we selected 17 samples among the 38 samples studied in Chauviré et al. (2017), based on the remaining materials from previous studies (Table A 1 in Appendix). Samples were sliced in thin sections, 150 to 350 µm thick, and polished on both sides for transmission acquisition. Among the 17 samples, 4 were opal-A and 13 were opal-CT. The type of opal (opal-CT and opal-A) was deduced from Raman spectroscopy, since it has been previously used to reliably classify opal and extensively used for this purpose. Raman spectroscopy is a non-destructive (no grinding required), a significant advantage in our study that focus on bulk samples (opal chips). Opal-A has a low-frequency T-O-T region-vibrational modes associated to bridging tetrahedron-oxygen-tetrahedron Si-O-Si- with a maximum near 430 cm^{-1}, whereas opal-CT has a maximum between 330-370 cm-1 (e.g. Ostrooumov et al., 1999). Homogeneity of each pieces used has been checked by measuring Raman spectra on a minimum of five points (300 µm radius), and pieces that show variations

in their structure have been discarded. Some opals are yellow to red (Table A 1), showing that they contain iron oxides and hydroxides as inclusions (Fritsch et al., 2002), however Raman and infrared spectra did not show any features characteristic of these components in our samples. Eight samples were analysed both at low pressure and low temperature (but independently), while other five samples were only exposed to low pressure, and four were exclusively used for low temperature experiments. To prevent potential irreversible changes, each piece has been used only for one type of experiment. Table 2 presents each sample and the respective exposure conditions.

2.2. Infrared spectra acquisition

Most of the near-infrared spectra were acquired using a Bruker Vertex 70 spectrometer coupled with a Bruker Hyperion 3000 microscope using a halogen lamp as source, an InGaAs detector and a CaF_2 beam splitter. Samples were placed in a cell (designed at the Institut de Planétologie et d'Astrophysique de Grenoble) with sapphire windows enabling transmission spectra, where the temperature and the pressure were lowered using, respectively, an internal circuit for liquid nitrogen and an air pump (HiCube, Pfeiffer). The sample was placed on a sapphire window enclosed in a core metallic piece acting as thermal exchanger either for cooling (by circulating liquid nitrogen) or heating (by two heating resistances). Schema of the experimental apparatus is available in Figure A 1 .

During low-pressure experiments, pressure was stabilized to between 7.2 to 10 millibars. The low pressure was maintained for a minimum period of one hour (for samples with no reaction visible in the spectra) or until a variation lower than 1% per minute between the acquired spectra and the previous one is observed in the OH and H_2O related absorptions (up to 21 hours).

Low-pressure experiments for samples 785, 1039, 1085, 1543d, 1552a, WT86 were performed using a Bruker Vertex 70V, which enables to have a vacuum in the sample

chamber of about 1 mbar, and to keep all the optical paths under the same condition. A detector InGaAs, with a CaF_2 beam splitter, and a tungsten halogen source equip this spectrometer.

Low-temperature experiments were all performed at ambient pressure; the gas in the cell was replaced by dry nitrogen, flushed during few minutes before maintaining ambient pressure. The sample was isolated from the external metal which was heated to 45 °C (318K) to avoid condensation, which was checked periodically by acquiring a "blank" spectrum (i.e. without the sample). The temperature was measured by a thermocouple PT100 inserted in the core metallic piece, close to the sapphire windows holding the sample (Figure A 1). The temperature was lowered to a range between -88°C to -95°C (185K to 178K; temperature given by the cell sensor). The exact temperature of the sample was estimated using the ice NIR features and its dependency with temperature, considering the effect of porosity depressing the water freezing point (more details are available in Appendix 1). Table 2 presents the temperature measured for the presented spectra, as well as temperature of the sample estimated through the aforementioned approach.

Each spectrum was an accumulation of 100 scans with a spectral resolution of 4 cm^{-1} and a beam size of 300x300 µm. Infrared spectra were acquired from 4000 to 10 000 cm^{-1}, but the focus was on the 4000 to 8000 cm^{-1} (2.5 µm to 1.25 µm) near-infrared spectral range, due to an important spectral artefact around 8300 cm^{-1}.

2.3. Laboratory Data Processing

The spectra's baselines were corrected using five anchor points located at the minimum absorptions near the 4200, 4700, 5400, 5700 and 7400 cm^{-1} wavelengths. For each anchor point, a Virtual Basic for Applications (VBA) program was developed to find the position of the local minimum in a 100 cm^{-1} region surrounding the anchor points defined above. Once

the minimum was found, a linear function was calculated between each anchor point. The functions were calculated and subtracted from the spectrum as shown in Appendix (Figure A 3). Both corrected and raw data are available in the open access SSHADE database (https://www.sshade.eu/ : https://doi.org/10.26302/SSHADE/EXPERIMENT_LB_20200201_001).

2.4. *Processing of CRISM hyperspectral images*

The Compact Reconnaissance Imaging Spectrometer for Mars (CRISM) on-board Mars Reconnaissance Orbiter (MRO) is a hyperspectral imaging spectrometer. It operates in the visible to NIR range from 0.36 µm to 3.92 µm through 544 channels with an average spectral resolution of about 6.55 nm (Murchie et al., 2007). CRISM data were derived from the TRR3 calibration (Seelos et al., 2011), and converted into surface reflectance signal by processing photometric and atmospheric gas absorptions using the empirical volcano-scan method (McGuire et al., 2009), as commonly used in previous work (e.g. Sun and Milliken, 2018).

Opaline silica was detected on Mars by adapting spectral parameters related to its specific absorption features (e.g. the 2.2 µm absorption - Viviano-Beck et al., 2014). Extraction of the spectra was then completed by using the methodology of Carter et al. (2013). Hydrated signatures were highlighted by subtracting a mean neutral spectral contribution (i.e. without the signature of hydrated phases) to hydrous mineral exposures over each observation. This method of extraction produces flat reflectance spectra close to a value of zero for spectrally neutral mineralogy. Arbitrary ratios of spectra of interest by spectra of selected neutral mineralogy were therefore not included, thus avoiding a process generally completed by the user. Spatial detection and localization of hydrated silica exposures were based on the spectral parameter BD2.25 introduced by Carter et al. (20013), which provides evidence of specific presence of hydrated silica within a CRISM scene. In a simplified way, this spectral parameter consists of the averaged band depth of the absorption band 2.25 µm, using moving

anchor points in the ranges 2.05-2.15 and 2.35-2.40 µm. Averaged spectra of opaline silica in the CRISM images were calculated by encompassing as many pixels as possible (up to several tens) to increase the signal-to-noise ratio.

2.5. Selection of Mars sites

To compare our results with Martian signature, three sites were selected based on (i) the quality of the available CRISM spectral cubes (*i.e.*, low dust content, satisfying atmospheric corrections, good signal-to-noise ratio) and (ii) the occurrence of spectrally "pure" opaline silica (*i.e.*, which spectra do not show any additional spectral absorption, indicating the presence of other hydrated phases). These sites were: (1) The Antoniadi crater region, (2) the Iani Chaos region, and (3) the Camichel crater.

In the Antoniadi crater region, opaline silica-rich materials formed aeolian accumulation (i.e. dunes) of crystalline silica phase around the central peaks of the impact craters, where zeolites and Fe/Mg-smectites or chlorites were detected (Ehlmann et al., 2009). It is suggested that the Antoniadi crater silica represents the erosional product of silica-rich materials altered by either hydrothermal activity of the crust under alkaline conditions or diagenetic processes in the subsurface (Ehlmann et al., 2009; Smith and Bandfield, 2012; Pineau et al., 2020).

The geomorphological context of Iani Chaos hydrated silica is reminiscent of the observations made for Antoniadi crater: *i.e.*, in aeolian dunes around the central peak of an impact crater. Fe/Mg-smectites (or chlorites) and hydrated sulfates are also detected on the crater rims and walls (Thomas et al., 2017). Iani Chaos silica-rich materials have been suggested to have been formed though similar geological processes as those of the Antoniadi crater (Pineau et al., 2020).

In the Camichel crater, hydrated silica was detected within light-toned materials in the distal part of an intra-crater fan delta. These silica-rich deposits are less crystalline than the deposits detected at Antoniadi crater or Iani Chaos and are interpreted as being formed in-situ during

delta formation or as product of continental weathering of deltaic silicic materials (Carter et al., 2012; Hauber et al., 2013; Pan et al., 2021; Pineau et al., 2020).

3. Results

3.1. Low pressure effects

Among the thirteen opals exposed to low pressure (all spectra available in Figure 1, and the evolution of the parameters of the bands are displayed in Figure 2), six opals reacted. In Figure 1, a lower Signal-to-Noise Ratio (SNR) is observed near 5400 cm^{-1} and 7300 cm^{-1}, due to the variations in the uniformity of the purge during pumping. An example of the evolution of bands with time is shown in Figure 3. Only one opal-A (86.2) slightly dehydrated, and five opal-CT reacted significantly (from very strong for WT86 to weak for 1085). For reacting opals, the band area near 5200 cm^{-1} decreased strongly. Among the six reacting opals, two (i.e. 86.2 and 1085) displayed a weak reaction, with a decrease of the 5200 cm^{-1} absorption bands of less than 10% of the initial band area. The other four strongly reacting opals showed a decrease in this band between 50% and 70% of the initial band area. In addition, it was noticed that the low-frequency wing reduced more than the high-frequency component, inducing an increase of the ratio between the two components (5250 cm^{-1} /5100 cm^{-1}) from 2.4-2.9 to 3.3-4.0.

A strong reaction to the low pressure was associated to an increase of the band near 4500 cm^{-1} (from 35% to 67%), transforming the nearly flat band into a sharper asymmetrical band with a apparent maximum shifted toward 4570 cm^{-1}. However, the sample 86.2 showed a reduction of the 4500 cm^{-1} band, with no change in shape or apparent maximum. For sample 1085, this band was too weak to monitor its evolution. Similarly to the band at 5200 cm^{-1}, the 7000 cm^{-1} band waned, but with slighter changes in the proportion of its two components. Only the 86.2 sample showed a slight increase in such proportion, but this could be attributed to an increased noise in the spectra.

Interestingly, a band at 7315 cm^{-1}, present as a small shoulder in the spectra at ambient pressure, significantly increased the NIR spectra of samples VTB, YM12, WT86 and FT1111.

For VTB, the strengthening of such band was not sufficient to become the maximum. Evolution of silica's NIR features at low pressure observed herein were consistent with previous studies (Poitras et al., 2018; Rice et al., 2013; Sun, 2017; Sun and Milliken, 2018).

3.2. Low temperature effects

Spectra of all the 13 opals measured before and after exposure to low temperature are presented in Figure 4, and the evolution of the band parameters are displayed in Figure 5. All opals reacted strongly, with significant changes in the 5200 cm^{-1} and 7000 cm^{-1} bands. The 4500 cm^{-1} band showed no significant variations, except for those induced by the change in the 3300 cm^{-1} absorption band. The 4500 cm^{-1} band is actually located on the higher wavenumber edge of the main hydration band (3300 cm^{-1}; 3 µm) which shifts to lower wavenumbers with lower temperature (Cloutis et al., 2008). Opal-A and opal-CT exposed to low temperature in this study had different reactions. The 5200 cm^{-1} band in the opal-A samples showed no shift of the apparent maximum position, but displayed a rise of the low-frequency component, leading to a decrease of the ratio of the two components (5250/5100 cm^{-1} - 1.91/1.96 µm). Simultaneously, the low frequency component in the 7000 cm^{-1} regions rose, causing a shift of the apparent maximum toward lower frequencies. This shift of the low frequency component increased the gap between the two components. This region thus exhibits two defined bands: one band near 6650 cm^{-1}, and a second band near 7100 cm^{-1} (Figure 4), with a ratio 7100/6650 cm^{-1} (1.41/1.50 µm) greater than at ambient temperature.

Except for sample 521, which showed a behaviour similar to opal-A, the studied opal-CT show a different evolution. The 5200 cm^{-1} band substantially shifted toward lower frequency (approximately 200 cm^{-1}), with a small shoulder persisting for the high-frequency component (i.e. near 5250 cm^{-1}, Figure 4). Additionally, the band became symmetrical. A similar reaction was observed in the 7000 cm^{-1} regions: an increase of the low-frequency component, an in turn of the ratio 7100/6850 cm^{-1}, and a shift of the position of the apparent maximum, with a small remaining shoulder near 7100 cm^{-1} (sometimes not visible).

4. Discussion

4.1. Low pressure effects

Six samples (among thirteen) reacted at Mars simulated pressure. By contrast, previous studies showed that most opals dehydrate at low pressure (Poitras et al., 2018; Rice et al., 2013; Sun, 2017; Sun and Milliken, 2018). One of the explanations could be the difference in

257 the acquisition method (reflectance for previous studies, compared to transmission in this
258 study); however, the band shape and position used here to characterize the effect of pressure,
259 is not affected by the mode of acquisition (Pineau et al., 2020). Samples preparation also
260 differed from previous studies; opals are prepared as thin sections here, whereas opals were
261 grinded in other studies. The grinding increases the surface available and opens the water-
262 filled porosity, facilitating the release of water; an effect demonstrated by thermal methods
263 (Smallwood et al., 2008). It has been proposed to explain the difference of water content
264 measured between the instrument SAM (after grinding) and ChemCam (directly on
265 unprepared sample), aboard MSL rover (Rapin et al., 2018).
266 In the study of hydration state of minerals, the relative humidity (RH), referring to the ratio of
267 real water content in an atmosphere compared to the water content at saturation of the same
268 atmosphere, is a key parameter. Rice et al. (2013) and Sun (2017) have demonstrated that, at
269 high RH, opal rehydrates, and Sun (2017) demonstrated that at low RH, opal dehydrates. In
270 our experiments, we estimate the RH assuming a RH of the air-conditioned air (40%) at the
271 pressure of the experiments. In the first setup (using a Bruker Vertex 70V under a pressure of
272 approximately 1 mbar), we calculate a RH ≈ 0.04%, and a RH ≈ 0.32 % (at 8 mbar) for the
273 second setup. According to the previous studies, the low RH in our experiments should
274 involve a dehydration. However, seven samples did not lose water.
275 The maximum duration of our experiments was 21 hours, compared to previous studies that
276 exposed samples for days or months. Our samples reacted in the first hours, but our results
277 should be considered as a lower limit for duration. It appears that our observations are
278 consistent with previous studies (Poitras et al., 2018; Rice et al., 2013; Sun, 2017; Sun and
279 Milliken, 2018), demonstrating that one day of exposure could be sufficient to observe
280 spectral variations at Mars-relevant pressure if water loss is possible through opal's porosity.
281 In the literature, opaline silica exposed to low pressure showed a shift of the 7000 cm^{-1} band
282 (1.4 µm) toward greater frequencies, a decrease of the 5200 cm^{-1} (1.9 µm) band, and an

283 increase with a shift of the band at 4500 cm^{-1}/2.2µm (Poitras et al., 2018; Rice et al., 2013;
284 Sun, 2017; Sun and Milliken, 2018). The band shapes changed through narrowing of the high-
285 frequency component, and in combination with the decrease of the low frequency component
286 on all bands, this leads to a change in the ratio between the two components (Poitras et al.,
287 2018; Rice et al., 2013; Sun and Milliken, 2018). All position shifts mainly resulted from the
288 change in the proportion of each component of the band, the weakening of a component,
289 and/or the strengthening of the other component, implying a shift of the apparent maximum.
290 Our results are consistent with previous studies. Quantitatively, the shift of the position of the
291 apparent maximum of the 7000 cm^{-1}-band in reacting opal-CT is greater than observed by Sun
292 & Milliken (2018), but consistent with Poitras et al. (2018). Our study shows that
293 distinguishing both types of opals using the band near 7000 cm^{-1} (1.4 µm) is more challenging
294 than previously thought.
295 In Chauviré et al. (2017), it was proposed that opal-A could be distinguished from other
296 varieties using the position of the apparent maximum of the 5200 cm^{-1} (limit between 5240
297 and 5245 cm^{-1}). After exposure, the strongly reacting opal-CT has an apparent maximum
298 overlapping with the opal-A's position; hence the limit is more blurred than previously
299 defined, consistent with Pineau et al. (2020).
300 Three of our sensitive opal-CT samples (WT86, FT1111 and YM12) showed an apparent
301 maximum near 7300 cm^{-1} after dehydration, caused by the growth of the band at 7316 cm^{-1},
302 attributed to isolated silanols OH stretching, similar to silica gel after heating or low-pressure
303 treatment (Boboň et al., 2011; Christy, 2011, 2010; Milliken et al., 2008; Rice et al., 2013).
304 The emergence of the band near 7300 cm^{-1} is consistent with the change of shape of the band
305 at 4500 cm^{-1}, attributed to a combination of siloxane and silanol groups. The four strongly
306 reacting opals (VTB, WT86, FT1111 and YM12) showed a decreasing 4425/4510 cm^{-1}
307 (2.26/2.21 µm) ratio and an apparent maximum close to isolated silanols bands at 4579 cm^{-1}

(Christy, 2011, 2010); this is in agreement with previous studies (Poitras et al., 2018; Sun and Milliken, 2018).

All these changes demonstrate that water was extracted from pores for almost half of the analysed samples. No correlation between colour, and thus presence of iron, and reaction at low pressure was observed. Similarly, both types of opal reacted, which is consistent with previous observations. The discrepancies between reacting and none-reacting samples could arise from their microstructure. Opal displays a variety of microstructures (Fritsch et al., 2006, 2002; Gaillou et al., 2008) that changes according to the formation environments and/or aging (e.g. Herdianita et al., 2000). Liquid-like water in opal is trapped inside nanometres to micrometres size pores (Chauviré and Thomas, 2020; Thomas et al., 2013). The proportion between open and closed porosity (i.e., respectively, connected to atmosphere and isolated from it) could explain the varying behaviour observed. The role of the microstructure on the opal dehydration by low pressure should be a major consideration when collecting sample containing water as a possible return martian sample target. In any case, the presence of free H_2O-molecules clusters in silica phases samples could be identifiable based on the 1.4 and 1.9 µm bands, which can be monitored by Supercam/IRS or Micromega (Bibring et al., 2017; Maurice et al., 2021).

The loss of water induces changes in the silanol configuration, by increasing the number of isolated silanols as proposed in earlier studies (Poitras et al., 2018; Sun, 2017; Sun and Milliken, 2018). The emergence of the 7320 cm^{-1} and the rise of the band component near 4520 cm^{-1} demonstrate the increasing amount of isolated silanols. Water molecules, initially adsorbed into surficial silanols, are lost during low-pressure exposure and transform bonded silanols into isolated ones, inducing a rising of the 4520 cm^{-1} and 7320 cm^{-1} bands. The increase of the area of the 4500 cm^{-1} band could be associated to either the creation of silanol on opal surface or to a difference in the molar absorptivity between isolated and bonded silanols. Considering the condition of the experiments, i.e. at ambient temperature and

without any chemical treatments, silanol genesis is deemed unlikely (Christy, 2011; Kondo et al., 1992). Therefore, water releases at low pressure affects all bands of NIR spectra of opal (A or CT) directly (by loss of water molecules) or indirectly (by reconfiguring silanols).

4.2. Low temperature effects

Our results show a significant shift of the apparent maximum for the bands at 7000 cm^{-1} and 5200 cm^{-1}, a decrease of the ratio 5250/5100 cm^{-1} (1.91/1.96 µm) and an increase of the ratio between components constitutive of the 7000 cm^{-1} (1.4 µm). The shift of the 5200 cm^{-1} is greater for opal-CT (> 100cm^{-1}, except for sample 521) than opal-A, which can be explained by the difference in water molecules enclosed. Opal-CT has more liquid-like water molecules, as demonstrated by NIR and thermal analysis (Chauviré and Thomas, 2020; Langer and Flörke, 1974), whereas opal-A mostly contains water molecules in a single layer that do not freeze due to surficial interaction (Ishikiriyama et al., 1995; Landry, 2005). Consequently, more water molecules freeze in opal-CT than in opal-A, involving greater changes in the 5200 cm^{-1} bands. The reaction of opal-CT 521, similar to opal-A, could be explained by a lower amount of water molecules as multilayers compared to the opal-CT samples. Sample 521 can be differentiated from other opal-A samples by the local minimum between 5100 cm^{-1} and 5250 cm^{-1} (deeper in opal-A).

Molecular water enclosed in the nanometric pores of opal freezes if temperature is low enough, i.e. usually < -30°C (<243K) for most opals, but up to -47°C (226K) in some cases (Chauviré and Thomas, 2020; Thomas et al., 2020, 2013). The change in shape and position of the apparent maxima of bands at 5200 cm^{-1} and 7000 cm^{-1} is similar to frozen water (

Figure 6). At 4500 cm^{-1}, no change that can be attributed to silanol reconfiguration was observed. A slight change was visible, but it is likely due to the proximity of the 3-µm water band, evolving with the crystallization of water. At the same time, we did not observe the isolated silanols band near 7320 cm^{-1}, but a shallow band remained near 7100 cm^{-1}. Therefore, during low temperature experiments, no isolated silanols, as seen for low-pressure experiments, were created. This can be explained by the non-freezable layer of water

molecules on silica surface, due to surface interaction (Ishikiriyama et al., 1995; Landry, 2005). It is thus consistent with the absence of silanol reconfiguration. The remaining shoulder near 5250 cm^{-1} (1.91 µm) and the shallow band near 7100 cm^{-1}, attributed to molecular water bonded to silanols (Christy, 2011, 2010), are evidence of such non-freezable layer.

Rice et al. (2013) exposed 11 opals to -13°C (260K), and they observed results consistent with our study; water phase changed in most of their samples, with low-temperature spectra dominated by water ice. Freezing point of water enclosed in nanometres-sized porous materials, including opals, shifts toward lower temperatures according to the size of water-filled pores (Chauviré and Thomas, 2020; Ishikiriyama et al., 1995; Landry, 2005; Thomas et al., 2020, 2013). The presence of ice at -13°C demonstrates that their samples contained larger pores, but the temperature may not be sufficient to freeze water-clusters in smaller pores (Chauviré and Thomas, 2020; Thomas et al., 2020, 2013). In parallel, grinding the samples exposes them to water from the terrestrial atmosphere, which will inevitably adsorb at the surface of the grains, which is limited in our study by using silica chips. Also since samples were analysed through transmission, we are probing deeper in the sample compared to reflectance spectroscopy, which tends to analyse more surficial parts of the samples. Poitras et al. (2018) have subjected opal to low temperature in Winnipeg's Mars Environment chamber (Craig et al., 2001), but the specific temperature was not mentioned in their study. Nevertheless, Poitras et al. (2018) did not observe a crystallization of water. This can be explained by either the operating temperature being higher than the water phase changes (the operating temperature of ME is -25°C; Craig et al., 2001), or by the low pressure causing the removal of all molecular water that may freeze (phenomenon enhanced by the grinding effect). The final spectra after exposure (Poitras et al (2018)) had a 3000 cm^{-1} band (3 µm), characteristic of H_2O vibrations, and a low frequency wing of 5200 cm^{-1} band (1.9 µm), demonstrating that molecular water remained in the silica.

Our observations are consistent with the freezing of "liquid" water in opals, as observed by Rice et al. (2013) and Sun (2017). Additionally, Sun (2017) also observed a rehydration of opal at RH > 90%. In our experiment, the low-temperature (circa -90°C) required a small amount of water to reach saturation, and even with the water impurity in nitrogen gas cylinder (maximum at 5 ppm), the RH was expected to be near 100%. High-RH prevented dehydration of our sample that could occur at lower RH, and it could explain why all samples contained ice, and at the same time the lack of rehydration. The main difference between Sun (2017) and the present study could be the result of the grinding effect. It should also be noted that thermalization of samples is a key issue in reflectance studies under low temperature, in particular for powders which can be subjected to strong temperature gradients.

4.3. Implications for opal on Mars

We present in

Figure 7 a comparison between two representative spectra of opaline silica from our experiments and spectra acquired with CRISM at three locations on Mars: Antoniadi crater, Iani Chaos and Camichel crater.

The temperature of the surface during the acquisition has been estimated from the location and local time using the last version of the Martian Climate Database developed from the General Circulation Model (Forget et al., 1999). Details on location, local time and the deduced atmospheric conditions are displayed in Appendix (Table A 2). These conditions, i.e. between -28 and -43°C, are favourable for the crystallization of water in opals (Chauviré and Thomas, 2020; Thomas et al., 2013).

All martian spectra exhibit an asymmetrical band at 4500 cm^{-1} (2.2 µm), with a greater contribution of the high frequency component. This may suggest, according to the spectra acquired at low pressure (here and by Poitras et al., 2018 and Sun & Milliken, 2018), that opaline silica was dehydrated. In the Camichel crater, the significant band near 7250 cm^{-1} is

an additional evidence of strong dehydration, and its absence in other spectra suggests that other deposits have experienced a dehydration to a lesser extent.

All spectra exhibited a band near 5200 cm^{-1} (1.9 µm) with an apparent maximum between 5100 and 5250 cm^{-1}. In our spectra, the crystallization of ice inside opal induced either a shift of the maximum (for opal-CT except 521) or the increase of the low-frequency shoulder (for opal-A and 521). No significant shift is visible in the martian spectra, suggesting that not enough water crystallizes to become the main contributor, which is consistent with the dehydration features observed in the 4500 cm^{-1} and 7000 cm^{-1} regions.

On the other hand, spectra from Antoniadi crater and Iani Chaos showed absorptions between 6500 and 6750 cm^{-1}, which is characteristic of the presence of OH in water molecules (Table 1). According to the atmospheric conditions (between 5.9 and 7.5 mbar and -28 and -43 °C), and from the thermal data on opal (Chauviré and Thomas, 2020; Thomas et al., 2013), water is likely in ice form, explaining the shoulder centred near 5100 cm^{-1} (1.96 µm,

Figure 4) in Antoniadi crater and Iani Chaos spectra . The proximity of atmospheric carbon dioxide near 2 µm prevents the use of this shoulder only (Gerakines et al., 2005; Khayat et al., 2019). Nevertheless, the large band near 6650 cm^{-1} associated with the shoulder near 5100 cm^{-1} suggest the presence of a small amount of water-ice.

As commonly discussed for mineral detections on Mars, a mixture of mineral phases is likely detected. Other hydrated phases, like sulphates and zeolites, possess absorption bands in the same regions. Sulphates, like gypsum or alunite, have a clear absorption at 5715 cm^{-1} (1,75 µm; Carter et al., 2013a; Ehlmann et al., 2016), not observed in our spectra. In addition, zeolites have a very shallow absorption near 4500 cm^{-1} (2,2 µm), as opposed to opaline silica. In addition, Mg-sulfates such as hexahydrite, epsomite or kieserite, have complex 1.4 and 1.9 µm absorption features that overlap water ice absorptions (e.g., Dalton et al., 2005). Thus, the presence of small amounts of Mg-sulfates with opaline silica can be responsible for the spectral signatures that we observe. However, obvious spectral evidence for the presence of Mg-sulfates were not observed; this strengthens the hypothesis of opaline silica with water ice

formation inside its structure. In any case, clear absorptions other than silica and water species were not identified in this study.

Water-ice particle (that would be intimately mixed with silica) are not expected to be the source of the absorption feature observed. In the spectra presented here for the Antoniadi crater and Iani Chaos, ice is unlikely, considering their geographical position in the martian tropical zone (respectively at 21.3°N and 2.06°S), on flat surface inside craters during either spring or summer martian seasons. Detection of water frost is more common at low- and mid-latitudes, but only on polar-faced slopes during fall or winter (Carrozzo et al., 2009; Vincendon et al., 2010). Moreover, except for hydrated silica detections, none of the surroundings exhibit absorptions typical of ice. A contribution of water ice clouds could interfere with the detection (Vincendon et al., 2011), but during the selection of the CRISM images, we prevented this interference by highlighting the presence of water ice through the application of the BD1500_2 from Viviano-Beck et al. (2014): only images that did not present any feature of ice, potentially originating from water-ice clouds or surface frost, were used here.

Therefore, in the Antoniadi regions and Iani Chaos, the detection of hydrated silica showed a slight but visible contribution of ice, suggesting that ice is present in opal structure at the time of the detection. This implies that for these regions, in contrast to the Camichel crater, opaline silica more efficiently retains molecular water in its structure. Opaline silica showing the presence of water in the porosity could be an interesting target for exploring the aqueous history of Mars. In addition to this, opaline silica could be used as a potential sample return target and in turn an efficient way to collect martian water (possibly ancient, preserved since the precipitation of silica).

5. Conclusion

By comparing data from available opal samples and from water ice at the same temperature (from Grundy & Schmitt, 1997, 1998), this study demonstrated that opal-CT and water/ice spectra are very close for bands near 5200 cm^{-1} and 7000 cm^{-1} (1.9 and 1.4 µm) (

Figure 6). The main band which allows to differentiate opal from water is the 4500 cm^{-1} (2.2 µm) band, and the contributions at 7100 cm^{-1} and 5250 cm^{-1} (1.405 and 1.905 µm).

For the detection of opal on Mars, the variety of band shapes according to the type of silica needs to be considered (as showed in Chauviré et al., 2017). Most of the studies aiming to improve silica detection focus on the most amorphous silica phases (i.e. opal-A or volcanic glasses), whereas opal-CT could be the most challenging to decipher. Ice features do not interfere with a potential identification of the opal-type, as opal-A appears to have an apparent maximum at higher frequency (shorter wavelength) than opal-CT, with two distinct bands whereas opal-CT exhibits only one broad band.

It was observed that in the Antoniadi crater and Iani Chaos martian opaline silica have a spectrum consistent with the presence of ice in their structure. Our results show that some opals may preserve molecular water in their structure, even when exposed to Mars atmosphere conditions, and that opaline silica could be a prime target for future sample return missions.

6. Author contributions

Boris Chauviré: Conceptualization, Methodology, Data curation, Investigation, Writing – Original draft, Visualization. Maxime Pineau: Data curation, Resources, Writing – Review and editing, Visualization. Eric Quirico: Validation, Resources, Writing – Review and Editing. Pierre Beck: Validation, Resources, Writing – Review and Editing

7. Competing interests

The authors declare that they have no known competing financial interests or personal relationships that could have appeared to influence the work reported in this paper.

8. References

Bibring, J.-P., Hamm, V., Pilorget, C., Vago, J.L., the MicrOmega Team, 2017. The MicrOmega Investigation Onboard ExoMars. Astrobiology 17, 621–626. https://doi.org/10.1089/ast.2016.1642

Bibring, J.P., Langevin, Y., Gendrin, A., Gondet, B., Poulet, F., Berthé, M., Soufflot, A., Arvidson, R., Mangold, N., Mustard, J., Drossart, P., Erard, S., Fomi, O., Combes, M., Encrenaz, T., Fouchet, T., Merchiorri, R., Belluci, G.C., Altieri, F., Formisano, V., Bonello, G., Capaccioni, F., Cerroni, P., Coradini, A., Fonti, S., Kottsov, V., Ignatiev, N., Moroz, V., Titov, D., Zasova, L., Pinet, P., Douté, S., Schmitt, B., Sotin, C., Hauber, E., Hoffmann, H., Jaumann, R., Keller, U., Duxbury, T., Forget, F., 2005. Mars surface diversity as revealed by the OMEGA/Mars express observations. Science (80-.). 307, 1576–1581. https://doi.org/10.1126/science.1108806

Boboň, M., Christy, A.A., Kluvanec, D., Illášová, L., 2011. State of water molecules and silanol groups in opal minerals: a near infrared spectroscopic study of opals from Slovakia. Phys. Chem. Miner. 38, 809–818. https://doi.org/10.1007/s00269-011-0453-0

Carrozzo, F.G., Bellucci, G., Altieri, F., D'Aversa, E., Bibring, J.P., 2009. Mapping of water frost and ice at low latitudes on Mars. Icarus 203, 406–420. https://doi.org/10.1016/j.icarus.2009.05.020

Carter, J., Poulet, F., Bibring, J.-P.J.-P.P., Mangold, N., Murchie, S., 2013a. Hydrous minerals on Mars as seen by the CRISM and OMEGA imaging spectrometers: Updated global view. J. Geophys. Res. Planets 118, 831–858. https://doi.org/10.1029/2012JE004145

Carter, J., Poulet, F., Mangold, N., Ansan, V., Dehouck, E., Bibring, J.-P., Murchie, S.L., 2012. Composition of alluvial fans and deltas on Mars, in: 43rd Lunar Planet. Sci. Conf. p. 2.

Carter, J., Poulet, F., Murchie, S., Bibring, J.P., 2013b. Automated processing of planetary hyperspectral datasets for the extraction of weak mineral signatures and applications to

515 CRISM observations of hydrated silicates on Mars. Planet. Space Sci. 76, 53–67.
516 https://doi.org/10.1016/j.pss.2012.11.007
517 Chauviré, B., Rondeau, B., Mangold, N., 2017. Near infrared signature of opal and
518 chalcedony as a proxy for their structure and formation conditions. Eur. J. Mineral. 29,
519 409–421. https://doi.org/10.1127/ejm/2017/0029-2614
520 Chauviré, B., Thomas, P.S., 2020. DSC of natural opal: insights into the incorporation of
521 crystallisable water in the opal microstructure. J. Therm. Anal. Calorim. 140, 2077–
522 2085. https://doi.org/10.1007/s10973-019-08949-4
523 Christy, A.A., 2011. Near infrared spectroscopic characterisation of surface hydroxyl groups
524 on hydrothermally treated silica gel. Int. J. Chem. Environ. Eng. 2, 27–32.
525 Christy, A.A., 2010. New insights into the surface functionalities and adsorption evolution of
526 water molecules on silica gel surface: A study by second derivative near infrared
527 spectroscopy. Vib. Spectrosc. 54, 42–49. https://doi.org/10.1016/j.vibspec.2010.06.003
528 Cloutis, E.A., Craig, M.A., Kruzelecky, R. V., Jamroz, W.R., Scott, A., Hawthorne, F.C.,
529 Mertzman, S.A., 2008. Spectral reflectance properties of minerals exposed to simulated
530 Mars surface conditions. Icarus 195, 140–168.
531 https://doi.org/10.1016/j.icarus.2007.10.028
532 Craig, M., Cloutis, E.A., Mueller, T., 2001. ME ans mini-ME: two Mars environmental
533 simulation chambers for reflectance spectroscopy, in: Lunar and Planetary Institute
534 Science Conference Abstracts.
535 Curtis, N.J., Gascooke, J.R., Johnston, M.R., Pring, A., 2019. A Review of the Classification
536 of Opal with Reference to Recent New Localities. Minerals 9, 299.
537 https://doi.org/10.3390/min9050299
538 Czarnecki, S., Hardgrove, C., Gasda, P.J., Gabriel, T.S.J., Starr, M., Rice, M.S., Frydenvang,
539 J., Wiens, R.C., Rapin, W., Nikiforov, S., Lisov, D., Litvak, M., Calef, F., Gengl, H.,
540 Newsom, H., Thompson, L., Nowicki, S., 2020. Identification and Description of a

Silicic Volcaniclastic Layer in Gale Crater, Mars, Using Active Neutron Interrogation. J. Geophys. Res. Planets 125, 1–20. https://doi.org/10.1029/2019JE006180

Dalton, J.B., Prieto-Ballesteros, O., Kargel, J.S., Jamieson, C.S., Jolivet, J., Quinn, R., 2005. Spectral comparison of heavily hydrated salts with disrupted terrains on Europa. Icarus 177, 472–490. https://doi.org/10.1016/j.icarus.2005.02.023

Des Marais, D.J., Walter, M.R., 2019. Terrestrial Hot Spring Systems: Introduction. Astrobiology 19, 1419–1432. https://doi.org/10.1089/ast.2018.1976

Djokic, T., Van Kranendonk, M.J., Campbell, K.A., Walter, M.R., Ward, C.R., 2017. Earliest signs of life on land preserved in ca. 3.5 Ga hot spring deposits. Nat. Commun. 8, 16149. https://doi.org/10.1038/ncomms16149

Ehlmann, B.L., Mustard, J.F., Swayze, G. a., Clark, R.N., Bishop, J.L., Poulet, F., Des Marais, D.J., Roach, L.H., Milliken, R.E., Wray, J.J., Barnouin-Jha, O.S., Murchie, S.L., 2009. Identification of hydrated silicate minerals on Mars using MRO-CRISM: Geologic context near Nili Fossae and implications for aqueous alteration. J. Geophys. Res. 114, E00D08. https://doi.org/10.1029/2009JE003339

Ehlmann, B.L., Swayze, G.A., Milliken, R.E., Mustard, J.F., Clark, R.N., Murchie, S.L., Breit, G.N., Wray, J.J., Gondet, B., Poulet, F., Carter, J., Calvin, W.M., Benzel, W.M., Seelos, K.D., 2016. Discovery of alunite in Cross crater, Terra Sirenum, Mars: Evidence for acidic, sulfurous waters. Am. Mineral. 101, 1527–1542. https://doi.org/10.2138/am-2016-5574

Elzea, J.M., Rice, S.B., 1996. Tem and X-Ray Diffraction Evidence for Cristobalite and Tridymite Stacking Sequences in Opal. Clays Clay Miner. 44, 492–500. https://doi.org/10.1346/CCMN.1996.0440407

Fassett, C.I., Head, J.W., 2008. The timing of martian valley network activity: Constraints from buffered crater counting. Icarus 195, 61–89. https://doi.org/10.1016/j.icarus.2007.12.009

567 Fink, U., Larson, H.P., 1975. Temperature dependence of the water-ice spectrum between 1
568 and 4 microns: Application to Europa, Ganymede and Saturn's rings. Icarus 24, 411–
569 420. https://doi.org/10.1016/0019-1035(75)90058-5
570 Forget, F., Hourdin, F., Fournier, R., Hourdin, C., Talagrand, O., Collins, M., Lewis, S.R.,
571 Read, P.L., Huot, J.-P., 1999. Improved general circulation models of the Martian
572 atmosphere from the surface to above 80 km. J. Geophys. Res. Planets 104, 24155–
573 24175. https://doi.org/10.1029/1999JE001025
574 Fritsch, E., Gaillou, E., Rondeau, B., Barreau, A., Albertini, D., Ostroumov, M., 2006. The
575 nanostructure of fire opal. J. Non. Cryst. Solids 352, 3957–3960.
576 https://doi.org/10.1016/j.jnoncrysol.2006.08.005
577 Fritsch, E., Ostrooumov, M., Rondeau, B., Barreau, A., Albertini, D., Marie, A.-M., Lasnier,
578 B., Wery, J., 2002. Mexican Gem Opals : nano- and micro-structure, origin of colour,
579 comparison woth other common opals of gemological significance. Aust. Gemol. 21,
580 230–233.
581 Fritsch, E., Rondeau, B., Hainschwang, T., Karampelas, S., 2012. Raman spectroscopy
582 applied to Gemmology, in: Raman Spectroscopy Applied to Earth Sciences and Cultural
583 Heritage. European Mineralogical Union, pp. 455–489. https://doi.org/10.1180/EMU-
584 notes.12.13
585 Fröhlich, F., 2020. The opal-CT nanostructure. J. Non. Cryst. Solids 533, 119938.
586 https://doi.org/10.1016/j.jnoncrysol.2020.119938
587 Frydenvang, J., Gasda, P.J., Hurowitz, J.A., Grotzinger, J.P., Wiens, R.C., Newsom, H.E.,
588 Edgett, K.S., Watkins, J., Bridges, J.C., Maurice, S., Fisk, M.R., Johnson, J.R., Rapin,
589 W., Stein, N.T., Clegg, S.M., Schwenzer, S.P., Bedford, C.C., Edwards, P., Mangold, N.,
590 Cousin, A., Anderson, R.B., Payré, V., Vaniman, D., Blake, D.F., Lanza, N.L., Gupta,
591 S., Van Beek, J., Sautter, V., Meslin, P.-Y., Rice, M., Milliken, R., Gellert, R.,
592 Thompson, L., Clark, B.C., Sumner, D.Y., Fraeman, A.A., Kinch, K.M., Madsen, M.B.,

Mitrofanov, I.G., Jun, I., Calef, F., Vasavada, A.R., 2017. Diagenetic silica enrichment and late-stage groundwater activity in Gale crater, Mars. Geophys. Res. Lett. 1–9. https://doi.org/10.1002/2017GL073323

Gaillou, E., Fritsch, E., Aguilar-Reyes, B., Rondeau, B., Post, J., Barreau, A., Ostroumov, M., 2008. Common gem opal: An investigation of micro- to nano-structure. Am. Mineral. 93, 1865–1873. https://doi.org/10.2138/am.2008.2518

Gerakines, P.A., Bray, J.J., Davis, A., Richey, C.R., 2005. The Strengths of Near-Infrared Absorption Features Relevant to Interstellar and Planetary Ices. Astrophys. J. 620, 1140–1150. https://doi.org/10.1086/427166

Grundy, W.M., Schmitt, B., 1998. The temperature-dependent near-infrared absorption spectrum of hexagonal H2O ice. J. Geophys. Res. E Planets 103, 25809–25822. https://doi.org/10.1029/98JE00738

Grundy, W.M., Schmitt, B., 1997. NIR optical constants spectrum of H2O Ih crystal and H2O liquid from 20 to 293 K. SSHADE/GhoSST. https://doi.org/10.26302/SSHADE/EXPERIMENT_BS_20120924_011.V1

Hapke, B., 1993. Theory of Reflectance and Emittance Spectroscopy. Cambridge University Press, Cambridge. https://doi.org/10.1017/CBO9780511524998

Hauber, E., Platz, T., Reiss, D., Le Deit, L., Kleinhans, M.G., Marra, W.A., de Haas, T., Carbonneau, P., 2013. Asynchronous formation of Hesperian and Amazonian-aged deltas on Mars and implications for climate. J. Geophys. Res. Planets 118, 1529–1544. https://doi.org/10.1002/jgre.20107

Herdianita, N.R., Browne, P.R.L., Rodgers, K.A., Campbell, K.A., 2000. Mineralogical and textural changes accompanying ageing of silica sinter. Miner. Depos. 35, 48–62. https://doi.org/10.1007/s001260050005

Ishikiriyama, K., Todoki, M., Motomura, K., 1995. Pore Size Distribution Measurements of Silica Gels by Means of Differential Scanning Calorimetry. J. Colloid Interface Sci. 171,

103–111. https://doi.org/10.1006/jcis.1995.1155

Jones, J.B., Segnit, E.R., 1971. The nature of opal I. nomenclature and constituent phases. J. Geol. Soc. Aust. 18, 57–68. https://doi.org/10.1080/00167617108728743

Khayat, A.S.J., Smith, M.D., Guzewich, S.D., 2019. Understanding the water cycle above the north polar cap on Mars using MRO CRISM retrievals of water vapor. Icarus 321, 722–735. https://doi.org/10.1016/j.icarus.2018.12.024

Kondo, S., Igarashi, M., Nakai, K., 1992. The properties of silica surfaces treated at high pH. Colloids and Surfaces 63, 33–37. https://doi.org/10.1016/0166-6622(92)80066-B

Landry, M.R., 2005. Thermoporometry by differential scanning calorimetry: Experimental considerations and applications. Thermochim. Acta 433, 27–50. https://doi.org/10.1016/j.tca.2005.02.015

Langer, K., Flörke, O.W., 1974. Near infrared absorption spectra (4000-9000 cm-1) of opals and the role of “water” in these SiO2-nH2O minerals. Fortschritte der Mineral. 52, 17–51.

Maurice, S., Wiens, R.C., Bernardi, P., Caïs, P., Robinson, S., Nelson, T., Gasnault, O., Reess, J.M., Deleuze, M., Rull, F., Manrique, J.A., Abbaki, S., Anderson, R.B., André, Y., Angel, S.M., Arana, G., Battault, T., Beck, P., Benzerara, K., Bernard, S., Berthias, J.P., Beyssac, O., Bonafous, M., Bousquet, B., Boutillier, M., Cadu, A., Castro, K., Chapron, F., Chide, B., Clark, K., Clavé, E., Clegg, S., Cloutis, E., Collin, C., Cordoba, E.C., Cousin, A., Dameury, J.C., D’Anna, W., Daydou, Y., Debus, A., Deflores, L., Dehouck, E., Delapp, D., De Los Santos, G., Donny, C., Doressoundiram, A., Dromart, G., Dubois, B., Dufour, A., Dupieux, M., Egan, M., Ervin, J., Fabre, C., Fau, A., Fischer, W., Forni, O., Fouchet, T., Frydenvang, J., Gauffre, S., Gauthier, M., Gharakanian, V., Gilard, O., Gontijo, I., Gonzalez, R., Granena, D., Grotzinger, J., Hassen-Khodja, R., Heim, M., Hello, Y., Hervet, G., Humeau, O., Jacob, X., Jacquinod, S., Johnson, J.R., Kouach, D., Lacombe, G., Lanza, N., Lapauw, L., Laserna, J., Lasue, J., Le Deit, L., Le

Mouélic, S., Le Comte, E., Lee, Q.M., Legett, C., Leveille, R., Lewin, E., Leyrat, C., Lopez-Reyes, G., Lorenz, R., Lucero, B., Madariaga, J.M., Madsen, S., Madsen, M., Mangold, N., Manni, F., Mariscal, J.F., Martinez-Frias, J., Mathieu, K., Mathon, R., McCabe, K.P., McConnochie, T., McLennan, S.M., Mekki, J., Melikechi, N., Meslin, P.Y., Micheau, Y., Michel, Y., Michel, J.M., Mimoun, D., Misra, A., Montagnac, G., Montaron, C., Montmessin, F., Moros, J., Mousset, V., Morizet, Y., Murdoch, N., Newell, R.T., Newsom, H., Nguyen Tuong, N., Ollila, A.M., Orttner, G., Oudda, L., Pares, L., Parisot, J., Parot, Y., Pérez, R., Pheav, D., Picot, L., Pilleri, P., Pilorget, C., Pinet, P., Pont, G., Poulet, F., Quantin-Nataf, C., Quertier, B., Rambaud, D., Rapin, W., Romano, P., Roucayrol, L., Royer, C., Ruellan, M., Sandoval, B.F., Sautter, V., Schoppers, M.J., Schröder, S., Seran, H.C., Sharma, S.K., Sobron, P., Sodki, M., Sournac, A., Sridhar, V., Standarovsky, D., Storms, S., Striebig, N., Tatat, M., Toplis, M., Torre-Fdez, I., Toulemont, N., Velasco, C., Veneranda, M., Venhaus, D., Virmontois, C., Viso, M., Willis, P., Wong, K.W., 2021. The SuperCam Instrument Suite on the Mars 2020 Rover: Science Objectives and Mast-Unit Description, Space Science Reviews. The Author(s). https://doi.org/10.1007/s11214-021-00807-w

McGuire, P.C., Bishop, J.L., Brown, A.J., Fraeman, A. a., Marzo, G. a., Frank Morgan, M., Murchie, S.L., Mustard, J.F., Parente, M., Pelkey, S.M., Roush, T.L., Seelos, F.P., Smith, M.D., Wendt, L., Wolff, M.J., 2009. An improvement to the volcano-scan algorithm for atmospheric correction of CRISM and OMEGA spectral data. Planet. Space Sci. 57, 809–815. https://doi.org/10.1016/j.pss.2009.03.007

Milliken, R.E., Swayze, G.A., Arvidson, R.E., Bishop, J.L., Clark, R.N., Ehlmann, B.L., Green, R.O., Grotzinger, J.P., Morris, R.V., Murchie, S.L., Mustard, J.F., Weitz, C., 2008. Opaline silica in young deposits on Mars. Geology 36, 847. https://doi.org/10.1130/G24967A.1

Morris, R. V, Vaniman, D.T., Blake, D.F., Gellert, R., Chipera, S.J., Rampe, E.B., Ming,

671 D.W., Morrison, S.M., Downs, R.T., Treiman, A.H., Yen, A.S., Grotzinger, J.P.,
672 Achilles, C.N., Bristow, T.F., Crisp, J.A., Des Marais, D.J., Farmer, J.D., Fendrich, K. V,
673 Frydenvang, J., Graff, T.G., Morookian, J.-M., Stolper, E.M., Schwenzer, S.P., 2016.
674 Silicic volcanism on Mars evidenced by tridymite in high-SiO2 sedimentary rock at Gale
675 crater. Proc. Natl. Acad. Sci. 113, 7071–7076. https://doi.org/10.1073/pnas.1607098113
676 Murchie, S., Arvidson, R., Bedini, P., Beisser, K., Bibring, J.P., Bishop, J., Boldt, J.,
677 Cavender, P., Choo, T., Clancy, R.T., Darlington, E.H., Des Marais, D., Espiritu, R.,
678 Fort, D., Green, R., Guinness, E., Hayes, J., Hash, C., Heffernan, K., Hemmler, J.,
679 Heyler, G., Humm, D., Hutcheson, J., Izenberg, N., Lee, R., Lees, J., Lohr, D., Malaret,
680 E., Martin, T., McGovern, J.A., McGuire, P., Morris, R., Mustard, J., Pelkey, S., Rhodes,
681 E., Robinson, M., Roush, T., Schaefer, E., Seagrave, G., Seelos, F., Silverglate, P.,
682 Slavney, S., Smith, M., Shyong, W.J., Strohbehn, K., Taylor, H., Thompson, P.,
683 Tossman, B., Wirzburger, M., Wolff, M., 2007. Compact Connaissance Imaging
684 Spectrometer for Mars (CRISM) on Mars Reconnaissance Orbiter (MRO). J. Geophys.
685 Res. E Planets 112, 1–57. https://doi.org/10.1029/2006JE002682
686 Mustard, J.F., Murchie, S.L., Pelkey, S.M., Ehlmann, B.L., Milliken, R.E., Grant, J.A.,
687 Bibring, J.-P., Poulet, F., Bishop, J.L., Noe Dobrea, E.Z., Roach, L., Seelos, F.P.,
688 Arvidson, R.E., Wiseman, S., Green, R., Hash, C., Humm, D., Malaret, E., McGovern,
689 J.A., Seelos, K., Clancy, T., Clark, R., Des Marais, D.J., Izenberg, N., Knudson, A.,
690 Langevin, Y., Martin, T., McGuire, P., Morris, R., Robinson, M., Roush, T., Smith, M.,
691 Swayze, G., Taylor, H., Titus, T., Wolff, M., 2008. Hydrated silicate minerals on Mars
692 observed by the Mars Reconnaissance Orbiter CRISM instrument. Nature 454, 305–309.
693 https://doi.org/10.1038/nature07097
694 Ostrooumov, M., Fritsch, E., Lasnier, B., Lefrant, S., 1999. Spectres Raman des opales:
695 aspect diagnostique et aide à la classification. Eur. J. Mineral. 11, 899–908.
696 Pan, L., Carter, J., Quantin-Nataf, C., 2019. Hydrated silica in martian alluvial fans and deltas,

in: Goldschmidt Conference.

Pan, L., Carter, J., Quantin-Nataf, C., Pineau, M., Chauviré, B., Mangold, N., Le Deit, L., Rondeau, B., Chevrier, V., 2021. Voluminous silica precipitated from martian waters during late-stage aqueous alteration. Planet. Sci. J. accepted.

Pineau, M., Le Deit, L., Chauviré, B., Carter, J., Rondeau, B., Mangold, N., 2020. Toward the geological significance of hydrated silica detected by near infrared spectroscopy on Mars based on terrestrial reference samples. Icarus 347, 113706. https://doi.org/10.1016/j.icarus.2020.113706

Poitras, J.T., Cloutis, E.A., Salvatore, M.R., Mertzman, S.A., Applin, D.M., Mann, P., 2018. Mars analog minerals' spectral reflectance characteristics under Martian surface conditions. Icarus 306, 50–73. https://doi.org/10.1016/j.icarus.2018.01.023

Rampe, E.B., Ming, D.W., Blake, D.F., Bristow, T.F., Chipera, S.J., Grotzinger, J.P., Morris, R. V., Morrison, S.M., Vaniman, D.T., Yen, A.S., Achilles, C.N., Craig, P.I., Des Marais, D.J., Downs, R.T., Farmer, J.D., Fendrich, K. V., Gellert, R., Hazen, R.M., Kah, L.C., Morookian, J.M., Peretyazhko, T.S., Sarrazin, P., Treiman, A.H., Berger, J.A., Eigenbrode, J., Fairén, A.G., Forni, O., Gupta, S., Hurowitz, J.A., Lanza, N.L., Schmidt, M.E., Siebach, K., Sutter, B., Thompson, L.M., 2017. Mineralogy of an ancient lacustrine mudstone succession from the Murray formation, Gale crater, Mars. Earth Planet. Sci. Lett. 471, 172–185. https://doi.org/10.1016/j.epsl.2017.04.021

Rapin, W., Chauviré, B., Gabriel, T.S.J.S.J.J., McAdam, A.C.C., Ehlmann, B.L.L., Hardgrove, C., Meslin, P.-Y.Y., Rondeau, B., Dehouck, E., Franz, H.B.B., Mangold, N., Chipera, S.J.J., Wiens, R.C.C., Frydenvang, J., Schröder, S., 2018. In Situ Analysis of Opal in Gale Crater, Mars. J. Geophys. Res. Planets 123, 1955–1972. https://doi.org/10.1029/2017JE005483

Rice, M.S., Cloutis, E.A., Bell, J.F., Bish, D.L., Horgan, B.H., Mertzman, S.A., Craig, M.A., Renaut, R.W., Gautason, B., Mountain, B., 2013. Reflectance spectra diversity of silica-

723 rich materials: Sensitivity to environment and implications for detections on Mars. Icarus
724 223, 499–533. https://doi.org/10.1016/j.icarus.2012.09.021
725 Ruff, S.W., Campbell, K.A., Van Kranendonk, M.J., Rice, M.S., Farmer, J.D., 2020. The
726 Case for Ancient Hot Springs in Gusev Crater, Mars. Astrobiology 20, 475–499.
727 https://doi.org/10.1089/ast.2019.2044
728 Ruff, S.W., Farmer, J.D., 2016. Silica deposits on Mars with features resembling hot spring
729 biosignatures at El Tatio in Chile. Nat. Commun. 7, 13554.
730 https://doi.org/10.1038/ncomms13554
731 Ruff, S.W., Farmer, J.D., Calvin, W.M., Herkenhoff, K.E., Johnson, J.R., Morris, R. V., Rice,
732 M.S., Arvidson, R.E., Bell, J.F., Christensen, P.R., Squyres, S.W., 2011. Characteristics,
733 distribution, origin, and significance of opaline silica observed by the Spirit rover in
734 Gusev crater, Mars. J. Geophys. Res. 116, E00F23.
735 https://doi.org/10.1029/2010JE003767
736 Seelos, F.P., Murchie, S.L., Humm, D.C., Barnouin, O.S., Morgan, F., Taylor, H.W., Hash,
737 C., Team, C., 2011. CRISM data processing and analysis products update - Calibration,
738 correction and visualization. 42nd Lunar Planet. Sci. Conf. 1–2.
739 Smallwood, A.G., Thomas, P.S., Ray, A.S., 2008. Characterisation of the dehydration of
740 australian sedimentary and volcanic precious opal by thermal methods. J. Therm. Anal.
741 Calorim. 92, 91–95. https://doi.org/10.1007/s10973-007-8742-z
742 Smith, M.D., Bougher, S.W., Encrenaz, T., Forget, F., Kleinböhl, A., 2017. Thermal Structure
743 and Composition, in: The Atmosphere and Climate of Mars. pp. 42–75.
744 https://doi.org/10.1017/9781139060172.004
745 Smith, M.R., Bandfield, J.L., 2012. Geology of quartz and hydrated silica-bearing deposits
746 near Antoniadi Crater, Mars. J. Geophys. Res. 117, 1–24.
747 https://doi.org/10.1029/2011JE004038
748 Squyres, S.W., Arvidson, R.E., Ruff, S., Gellert, R., Morris, R. V., Ming, D.W., Crumpler, L.,

749 Farmer, J.D., Marais, D.J.D., Yen, A., McLennan, S.M., Calvin, W., Bell, J.F., Clark,
750 B.C., Wang, A., McCoy, T.J., Schmidt, M.E., de Souza, P.A., 2008. Detection of Silica-
751 Rich Deposits on Mars. Science (80-.). 320, 1063–1067.
752 https://doi.org/10.1126/science.1155429
753 Sun, V.Z., 2017. Clays and Opals on Mars : Implications for Water-Rock Interactions
754 Through Time. Brown University. https://doi.org/10.7301/Z08G8J58
755 Sun, V.Z., Milliken, R.E., 2018. Distinct Geologic Settings of Opal-A and More Crystalline
756 Hydrated Silica on Mars. Geophys. Res. Lett. 45, 10,221-10,228.
757 https://doi.org/10.1029/2018GL078494
758 Swayze, G.A., Milliken, R.E., Clark, R.N., Bishop, J.L., Ehlmann, B.L., Pelkey, S.M.,
759 Mustard, J.F., Murchie, S.L., Brown, A.J., Team, T.M.C., 2007. Spectral evidence for
760 hydrated volcanic and/or impact glass on Mars with MRO CRISM, in: Seventh
761 International Conference on Mars.
762 Tarnas, J.D., Mustard, J.F., Lin, H., Goudge, T.A., Amador, E.S., Bramble, M.S., Kremer,
763 C.H., Zhang, X., Itoh, Y., Parente, M., 2019. Orbital Identification of Hydrated Silica in
764 Jezero Crater, Mars. Geophys. Res. Lett. 46, 12771–12782.
765 https://doi.org/10.1029/2019GL085584
766 Teece, B.L., George, S.C., Djokic, T., Campbell, K.A., Ruff, S.W., Van Kranendonk, M.J.,
767 2020. Biomolecules from Fossilized Hot Spring Sinters: Implications for the Search for
768 Life on Mars. Astrobiology 20, 537–551. https://doi.org/10.1089/ast.2018.2018
769 Thomas, P., Chauviré, B., Flower-Donaldson, K., Aldridge, L., Smallwood, A., Liu, B., 2020.
770 FT-NIR and DSC characterisation of water in opal. Ceram. Int. 46, 29443–29450.
771 https://doi.org/10.1016/j.ceramint.2020.05.026
772 Thomas, P.S., Guerbois, J.-P., Smallwood, A.G., 2013. Low temperature DSC
773 characterisation of water in opal. J. Therm. Anal. Calorim. 113, 1255–1260.
774 https://doi.org/10.1007/s10973-012-2911-4

775 Thomas, R.J., Hynek, B.M., Osterloo, M.M., Kierein-Young, K.S., 2017. Widespread
776 exposure of Noachian phyllosilicates in the Margaritifer region of Mars: Implications for
777 paleohydrology and astrobiological detection. J. Geophys. Res. Planets 122, 483–500.
778 https://doi.org/10.1002/2016JE005183
779 Vincendon, M., Forget, F., Mustard, J., 2010. Water ice at low to midlatitudes on Mars. J.
780 Geophys. Res. E Planets 115, 1–13. https://doi.org/10.1029/2010JE003584
781 Vincendon, M., Pilorget, C., Gondet, B., Murchie, S., Bibring, J.P., 2011. New near-IR
782 observations of mesospheric CO2 and H2O clouds on Mars. J. Geophys. Res. E Planets
783 116, 1–18. https://doi.org/10.1029/2011JE003827
784 Viviano-Beck, C.E., Seelos, F.P., Murchie, S.L., Kahn, E.G., Seelos, K.D., Taylor, H.W.,
785 Taylor, K., Ehlmann, B.L., Wisemann, S.M., Mustard, J.F., Morgan, M.F., Wiseman,
786 S.M., Mustard, J.F., Morgan, M.F., 2014. Revised CRISM spectral parameters and
787 summary products based on the currently detected mineral diversity on Mars. J.
788 Geophys. Res. E Planets 119, 1403–1431. https://doi.org/10.1002/2014JE004627
789 Weitz, C.M., Milliken, R.E., Grant, J. a., McEwen, a. S., Williams, R.M.E., Bishop, J.L.,
790 Thomson, B.J., 2010. Mars Reconnaissance Orbiter observations of light-toned layered
791 deposits and associated fluvial landforms on the plateaus adjacent to Valles Marineris.
792 Icarus 205, 73–102. https://doi.org/10.1016/j.icarus.2009.04.017
793 Wilson, M.J., 2014. The structure of opal-CT revisited. J. Non. Cryst. Solids 405, 68–75.
794 https://doi.org/10.1016/j.jnoncrysol.2014.08.052
795

9. Figures captions

Figure 1 (single column): Near infrared spectra of samples used in this study before (black) and after (green) exposure to low pressure. Spectra has been offset for clarity.

Figure 2 (1.5 column): Evolution of the parameters for each band (a: 4500cm^{-1}, b: 5200 cm^{-1}, c: 7000 cm-1) between ambient conditions (black filled) and after low-pressure exposition (empty green symbols). Each plot represents the evolution of the ratio of the two components of the band versus the apparent maximum. Reacting samples are shown with an arrow between the initial state and after exposition. Circles represent opal-A sample and triangles opal-CT. For the band at 4500 cm^{-1}, only reacting samples with a variation greater than 10% in area (implying a variation on other parameters) have been represented to improve readability.

Figure 3 (single column): evolution of bands with time during exposure to low pressure for opal-CT WT86. Shown spectra were acquired at room temperature every 30 minutes, demonstrating a strong evolution during the first hours. The last spectrum was acquired 16h45 after the beginning of the experiment.

Figure 4 (single column): Spectra before (grey) and after (blue) exposure to low temperature (applied temperatures are noted in Table 2). Spectra has been offset for clarity.

Figure 5 (1.5 column): Evolution of parameter of the band at 5200 cm^{-1} (a) and 7000 cm^{-1} (b); with the ratio of the two components versus the position of the apparent maximum. In black, parameters at room temperature and in blue at low temperature (temperature given in Table 2). Circles represent opal-A samples, and triangles opal-CT.

Figure 6 (single column): Absorption spectra of water (solid line) and an opal-CT (1543b; dotted line) at both room temperature (black line; 293.5 K) and low temperature (blue line; 180K measured and 220K from calibrated temperature for opal, 230 K for water). Data for water was extracted from Grundy & Schmitt (1997). Y-axis was normalized and offset for clarity.

Figure 7 (single column): Continuum removed CRISM spectra from three locations where opaline silica was identified (Antoniadi crater, Iani Chaos region and Camichel crater) compared to the laboratory spectra acquired at similar temperature. To improve the comparison, the reflectance spectra of terrestrial opal has been simulated from transmission spectra according to Hapke model (Hapke, 1993). Blue areas indicate water ice regions and vertical dotted line indicates absorptions bands specific to hydrated silica. The penultimate spectrum is a CRISM spectrum of water ice at the northern cap of Mars to make comparison with the 1551 opal-CT sample. The last one is a montmorillonite spectrum from the USGS dataset showing a 4500 cm^{-1} absorption band narrower than opaline silica.

Band positions cm^{-1} (µm)	Band attributions	Vibration mode
4420 (2.26)	Combination of OH stretching (hydrogen bonded to water molecules) and siloxane (Si-O-Si) bending	$\delta_{SiOH} + \upsilon_{OH}$
4500 (2.21)	Combination of free OH stretching (not hydrogen bonded to water molecules) and siloxane (Si-O-Si) bending	$\delta_{SiOH} + \upsilon_{OH}$
5100 (1.96)	Combination of OH stretching and bending in water molecules (hydrogen bonded)	$\upsilon_2 + \upsilon_3$
5250 (1.91)	Combination of OH stretching and bending in water molecules (free)	$\upsilon_2 + \upsilon_3$
6850 (1.46)	Combination of OH stretching and bending in water molecules (hydrogen bonded)	$2\upsilon_2 + \upsilon_{3*}$ $2\upsilon_{3*}$ $\upsilon_1 + \upsilon_{3*}$
7090 (1.41)	OH stretching in silanols	$2\upsilon_{OH}$

10. Tables

Table 1 : NIR absorptions (between 4000 and 8000 cm^{-1}) of molecular water (H_2O_{mol}), silanol groups (SiOH) and OH in amorphous silica (after Anderson & Wickersheim 1964; Flörke et al., 1982; Kronenberg, 1994). Vibration mode: δ_{SiOH} = SiOH bending in plane; υ_{OH} = OH-stretching; υ_2 = symmetric bending; υ_3 = antisymmetric stretching. *The attribution of the band at 6580 cm^{-1} (1.46 µm) is debated.

Sample	Variety	Mars simulated			
		Pressure		Temperature (°C)	
		Measured (mbar)	Time (h:min)	Measured	Sample
86.2	Opal-A	7.21	4:10	-90.4	-88.9
785		1	17:10	-89.8	-89
1039		1	2:40		
1040		7.2	1:00	-91	-81.1
521	Opal-CT			-91.6	-51.1
1085		1	5:35	-90.8	-62.9*
1543a				-89.2	-64.2*
1543b		7.36	3:40	-94	-87.8*
1543d		1	2:00	-88.1	-57.7
1548				-89.2	-68.9*
1551		7.25	14:20	-91.6	-57.2
1552a		1	2:50	-94	-96.5*
1552b				-92.5	-78.1*
WT86		1	16:45		
FT1111		7.85	21:00		
VTB		7.24	20:00		
YM12		10	1:50		

Table 2 **:** Samples used for the experiments at Mars-relevant pressure and temperature. The column "Measured" is the temperature measured by the sensor in the cell, the column "Sample" is the temperature calculated from the calibration based on the NIR ice bands. *indicates the sample used to recalculate the calibration from Fink & Larson (1975) to take account of the onset temperature. The other sample's temperature has been calculated using the recalculated calibration by taking account of the onset temperature from the DSC measurements available (Chauviré and Thomas, 2020).

11. Appendix

11.1. Temperature of sample

As the sample is placed on a sapphire window (to acquire transmission spectra), and the temperature sensor is located on the surrounding freezing circuit, a difference between the temperature of the sample and the sensor exists. As water in opal could freeze at low temperature, we used the temperature dependency of the 5500-7000 cm^{-1} (1.82-1.43 µm) region of water ice (Fink and Larson, 1975; Grundy and Schmitt, 1998) to estimate the exact temperature of the sample (consequently, this method is only applicable when ice is present in the sample). The area of the shoulder near 6050 cm^{-1} divided by all the area between 5500 cm^{-1} and 7000 cm^{-1} is dependent of the temperature of the ice (Appendix Figure A 2): the larger the ratio is, the lower the temperature is (Fink and Larson, 1975). Given that our spectra were acquired above 100K, it avoids the unreliability of this calibration at lower temperatures (Grundy and Schmitt, 1998). In addition, the crystallization of water in opals demonstrates that this amount of water did not interact with the silica surface, or silanols linked to it (Ishikiriyama et al., 1995; Landry, 2005). Fink & Larson (1975) established the following linear equation:

$$T = -2862 * R_{\frac{6050}{6600}} - 2.15$$

Where T is the temperature in °C, and $R_{\frac{6050}{6600}}$ is the ratio between the area of the 6050 cm^{-1} band and the area of the 5500-7000 cm^{-1} region.

As the water trapped inside nanometric pores freezes at lower temperature due to surficial interaction, the temperature deducted from ice-related NIR bands needs to be corrected from the freezing point depression. In Chauviré and Thomas (2020), the six samples used to recalculate the calibration (1085, 1543a, 1543b, 1548, 1552a, 1552b) have been analyzed by low-temperature Differential Scanning Calorimetry (DSC), and the onset temperature (corresponding to the start of water freezing) has been added to the calibrated temperature. Based on the measured temperature, the temperature from the calibration and the onset temperature, we established a calibration equation as below:

$$T_m = 5.518 * (T_c + \Delta T_{on}) + 429.14$$

Where T_m is the measured temperature, T_c is the temperature from the Fink and Larson (1975) calibration and ΔT_{on} is the onset temperature, with a $R^2 = 0.81$.

11.2. Figures captions

Figure A 1 : Schematics of the cell used to analyse at Mars-relevant conditions.

Figure A 2: Area of bands used for the temperature calibration. NIR spectrum of pure ice from Gundry & Schmidt (1998) at 180 K (-93 °C).

Figure A 3 : Process used to remove the baseline from the spectra (here shown for opal 86.2)

Sample	Variety	Color	Origin	
			Geographic	Geological
86.2	Opal-A	White	Kashau, Slovakia	Unknown
785		White	Honduras	Unknown
1039		Orange	Mintabie, South Australia, Australia	Weathering
1040		Grayish-yellow	Coober Pedy, South Australia, Australia	Weathering
521	Opal-CT	Dark brown	Mezezo, Ethiopia	Hydrothermal
1085		Greenish yellow	"New Maternal", Argentina	Unknown
1543a		Red	San Martin, Jalisco, Mexico	Hydrothermal
1543b		Brownish red		
1543d		Orange		
1548		White	Fougères, Brittany, France	Unknown
1551		Dark brown	Mezezo, Ethiopia	Hydrothermal
1552a		Red	Guadalupana, Nayarit, Mexico	Hydrothermal
1552b		Orange red		
WT86		Light orange	Wegel Tena, Ethiopia	Weathering
FT1111		Whitish orange		
VTB		White		
YM12		Orange	Mezezo, Ethiopia	Hydrothermal

11.3. Tables

Table A 1 : Characteristic and origin of the samples used in this study.

Region	CRISM ID scene	Center Lat/Long	Terrestrial observation time	Solar longitude Ls	Martian observation time	Surface temperature	Surface pressure
Antoniadi crater	FRT00009312_07_IF166L_TRR3	19.92°N. 65.86°E	2008-01-04 @14:02 UT	12.6°	MY29. MM01/12. sol 026/669 @08:56 LTST	230.5 K (-42.7°C)	5.9 mbar
	FRT00009BCE_07_IF166L_TRR3	18.52°N. 65.14°E	2008-02-01 @07:51 UT	25.7°	MY29. MM01/12. sol 053/669 @09:25 LTST	244.9 K (-28.3°C)	6.0 mbar
Iani Chaos	FRT000134D2_07_IF165L_TRR3	-0.61°N. -18.03°E	2009-06-19 @01:02 UT	287.7°	MY29. MM10/12. sol 543/669 @17:24 LTST	245.6 K (-27.5°C)	7.5 mbar
Camichel crater	HRL0000985E_07_IF182L_TRR3	2.71°N. -51.66°E	2008-01-19 @07:26 UT	19.6°	MY29. MM01/12. sol 040/669 @09:20 LTST	237.0 K (-36.2°C)	6.9 mbar

Table A 2 : Details of martian hydrated silica spectra and estimations of surface conditions from the GCM. UT = Universal Time.

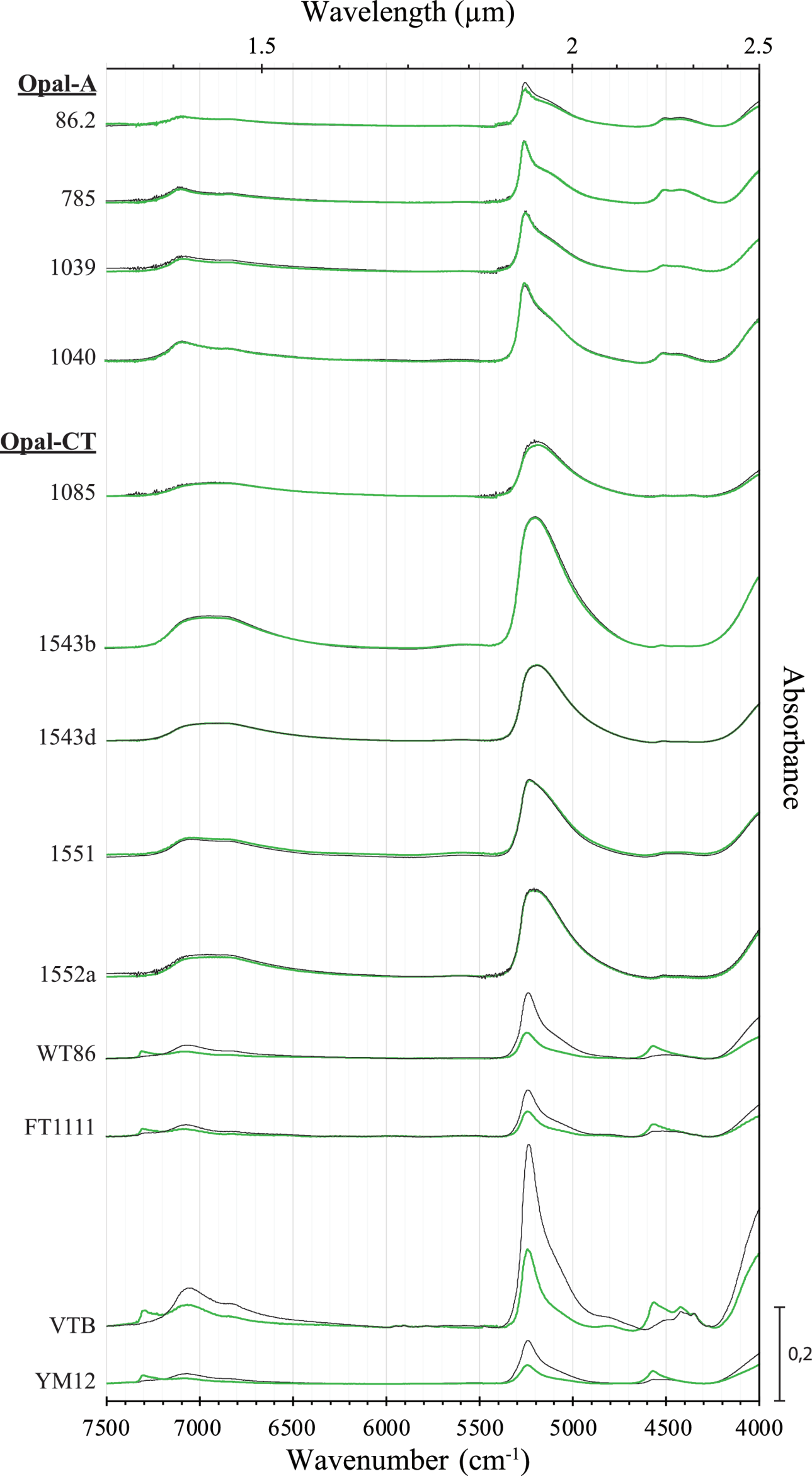
Wavelength (µm)
1.5
2
2.5
Opal-A
86.2
785
1039
1040
Opal-CT
1085
1543b
1543d
1551
1552a
WT86
FT1111
VTB
YM12
Absorbance
0,2
7500
7000
6500
6000
5500
5000
4500
4000
Wavenumber (cm-1)

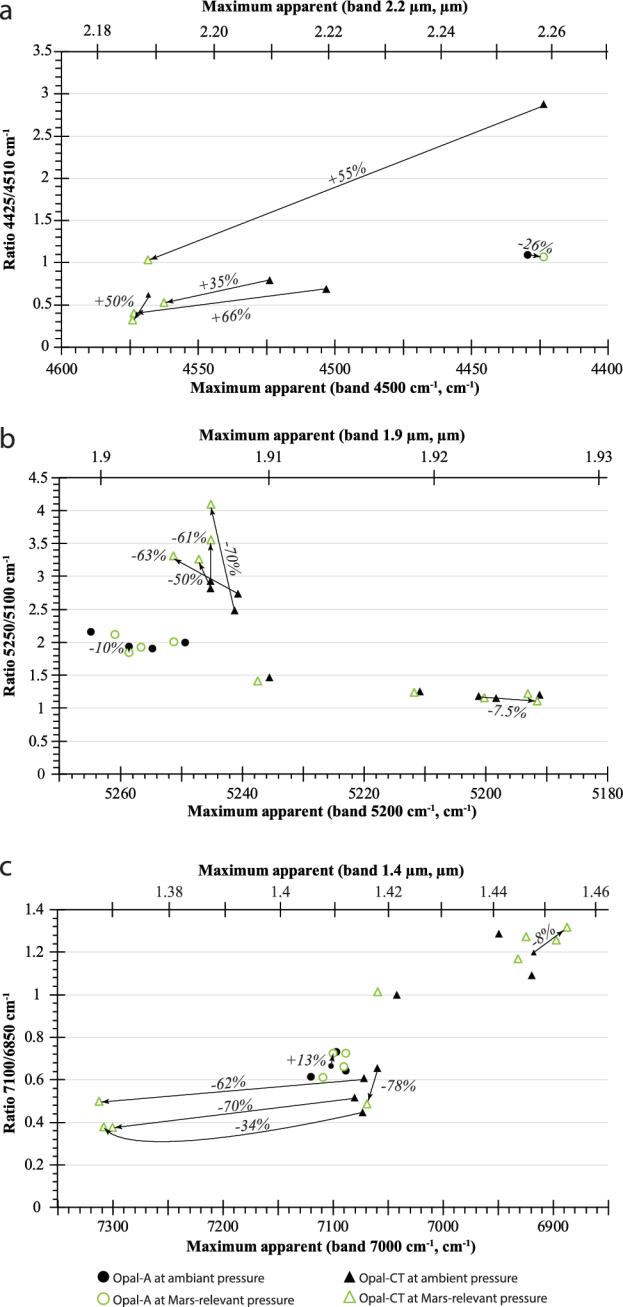
a
Maximum apparent (band 2.2 µm, µm)
2.18
2.20
2.22
2.24
2.26
Ratio 4425/4510 cm-1
3.5
3
2.5
2
1.5
1
0.5
0
+55%
-26%
+35%
+50%
+66%
4600
4550
4500
4450
4400
Maximum apparent (band 4500 cm-1, cm-1)
b
Maximum apparent (band 1.9 µm, µm)
1.9
1.91
1.92
1.93
Ratio 5250/5100 cm-1
4.5
4
3.5
3
2.5
2
1.5
1
0.5
0
-61%
-70%
-63%
-50%
-10%
-7.5%
5260
5240
5220
5200
5180
Maximum apparent (band 5200 cm-1, cm-1)
c
Maximum apparent (band 1.4 µm, µm)
1.38
1.4
1.42
1.44
1.46
Ratio 7100/6850 cm-1
1.4
1.2
1
0.8
0.6
0.4
0.2
0
-8%
+13%
-62%
-78%
-70%
-34%
7300
7200
7100
7000
6900
Maximum apparent (band 7000 cm-1, cm-1)
Opal-A at ambiant pressure
Opal-CT at ambient pressure
Opal-A at Mars-relevant pressure
Opal-CT at Mars-relevant pressure

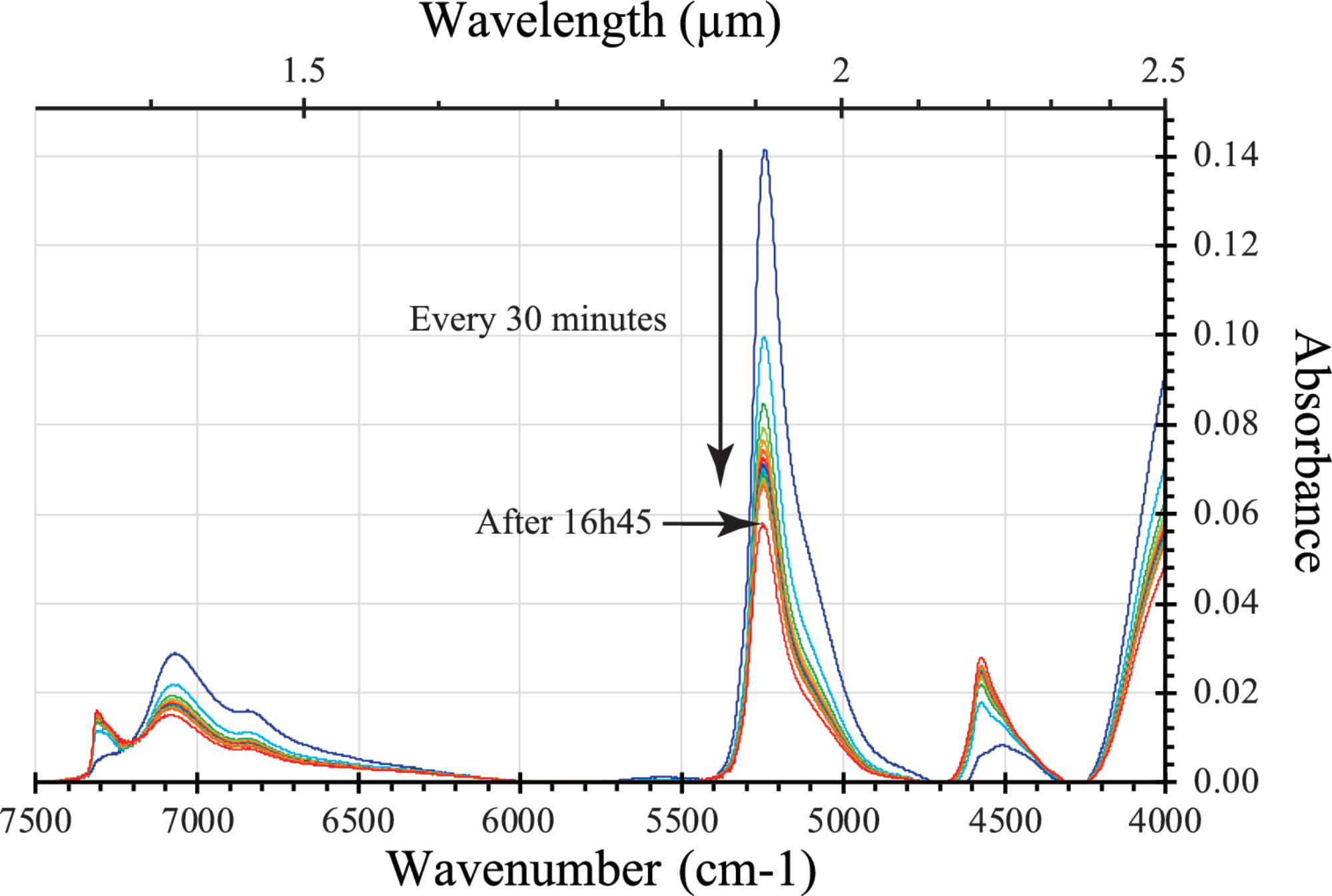
Wavelength (µm)
1.5
2
2.5
Every 30 minutes
After 16h45
0.14
0.12
0.10
0.08
0.06
0.04
0.02
0.00
Absorbance
7500
7000
6500
6000
5500
5000
4500
4000
Wavenumber (cm-1)

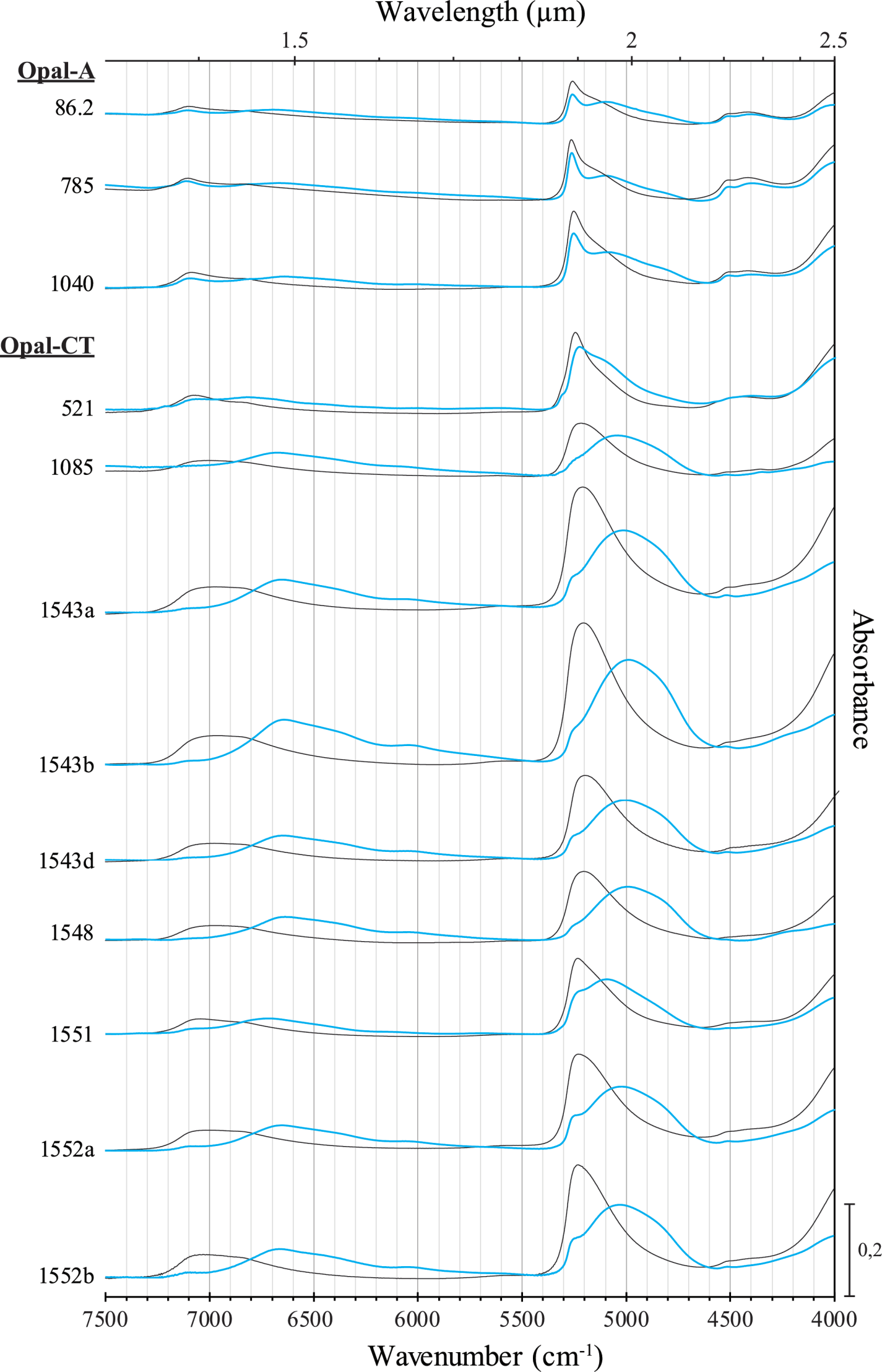
Wavelength (µm)
1.5
2
2.5
Opal-A
86.2
785
1040
Opal-CT
521
1085
1543a
1543b
1543d
1548
1551
1552a
1552b
Absorbance
0,2
7500
7000
6500
6000
5500
5000
4500
4000
Wavenumber (cm-1)

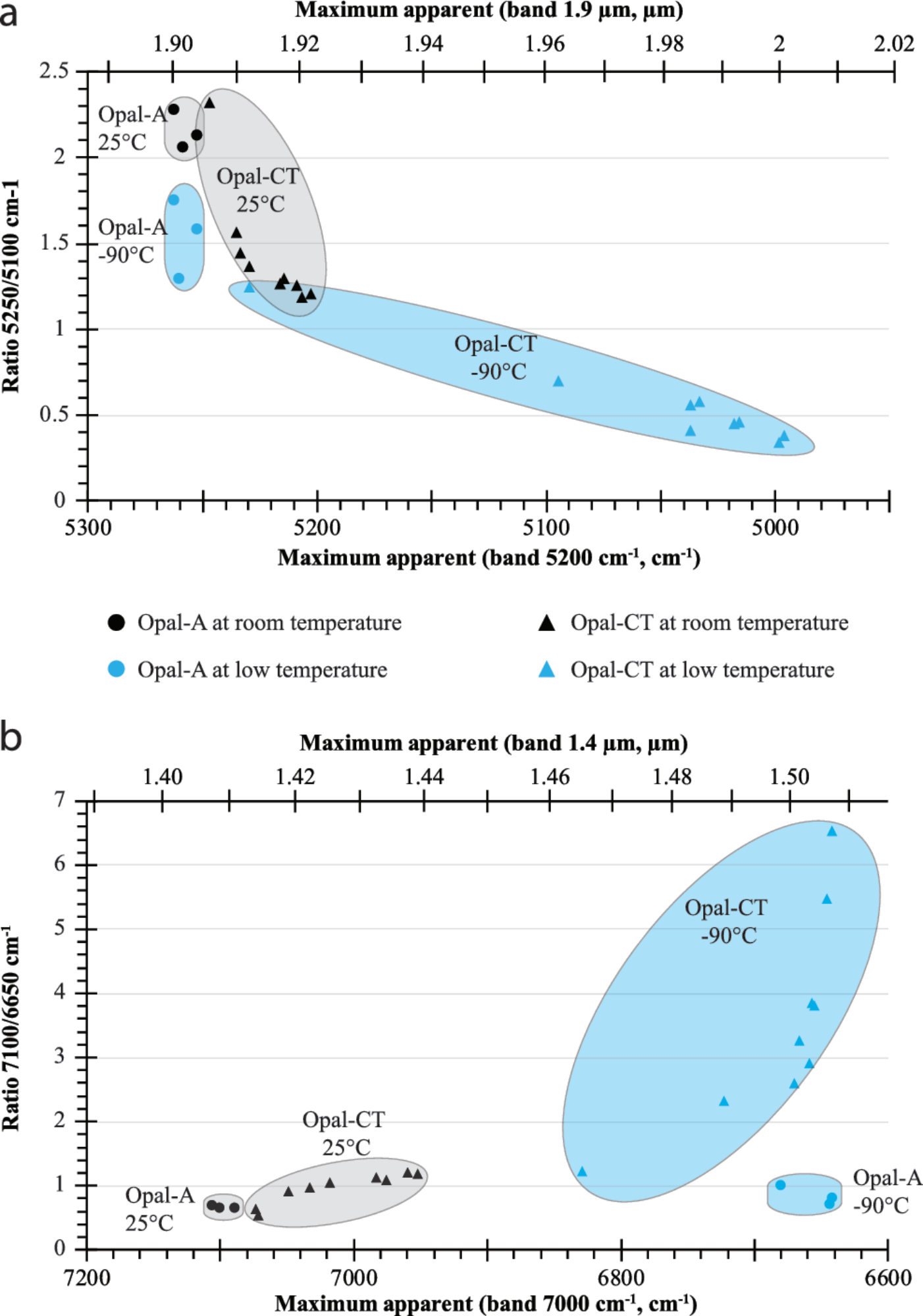
a
Maximum apparent (band 1.9 µm, µm)
1.90
1.92
1.94
1.96
1.98
2
2.02
2.5
2
1.5
1
0.5
0
Ratio 5250/5100 cm-1
Opal-A
25°C
Opal-CT
25°C
Opal-A
-90°C
Opal-CT
-90°C
5300
5200
5100
5000
Maximum apparent (band 5200 cm-1, cm-1)
Opal-A at room temperature
Opal-CT at room temperature
Opal-A at low temperature
Opal-CT at low temperature
b
Maximum apparent (band 1.4 µm, µm)
1.40
1.42
1.44
1.46
1.48
1.50
7
6
5
4
3
2
1
0
Ratio 7100/6650 cm-1
Opal-CT
-90°C
Opal-CT
25°C
Opal-A
25°C
Opal-A
-90°C
7200
7000
6800
6600
Maximum apparent (band 7000 cm-1, cm-1)

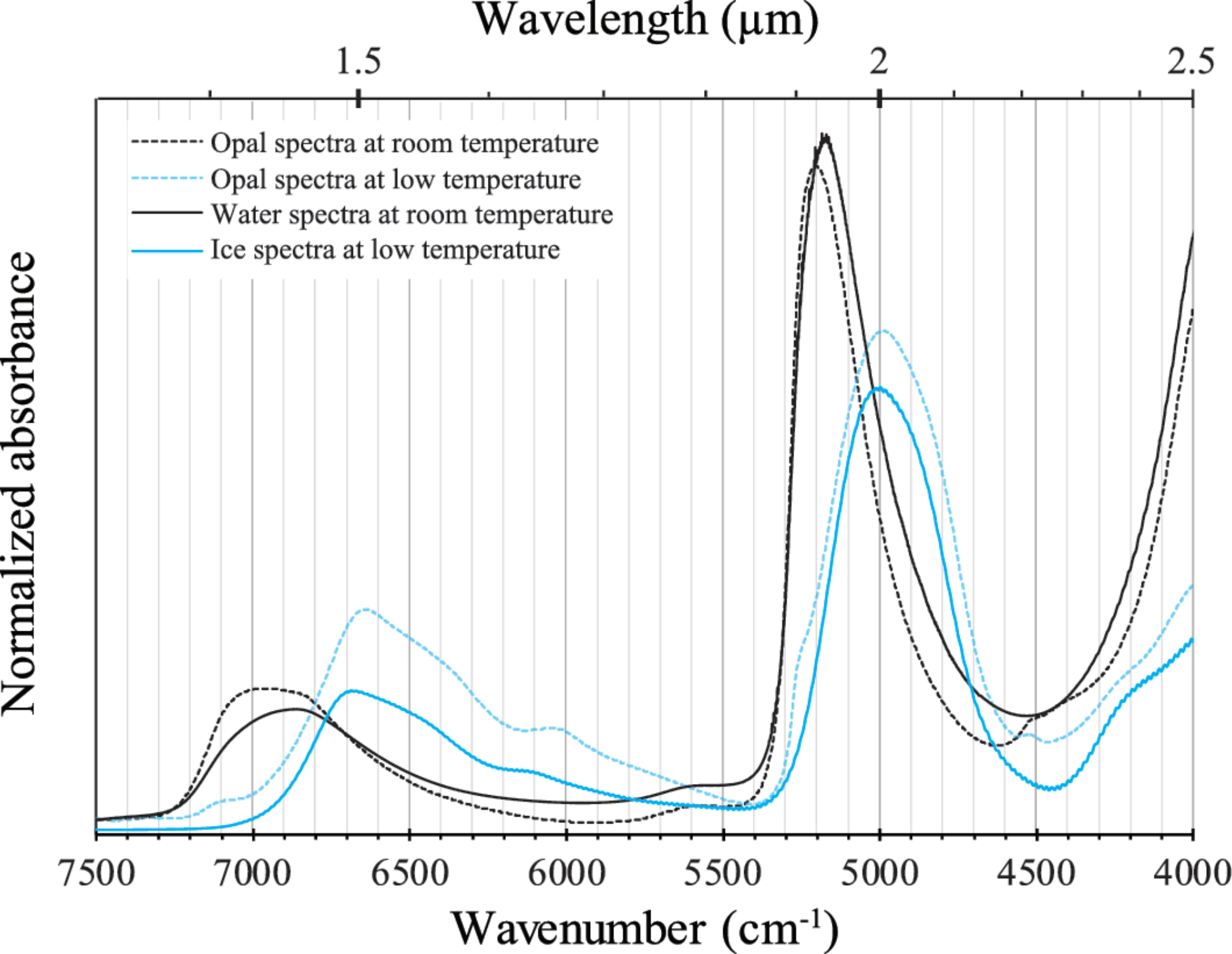
Wavelength (μm)
1.5
2
2.5
Opal spectra at room temperature
Opal spectra at low temperature
Water spectra at room temperature
Ice spectra at low temperature
Normalized absorbance
7500
7000
6500
6000
5500
5000
4500
4000
Wavenumber (cm-1)

Wavelength (µm)

1.4 1.6 1.8 2.0 2.2 2.4

spectral artifacts

CO_2 absorptions

Ratioed I/F CRISM normalized reflectance (continuum removed spectra)

1.00 0.80 0.60 0.40 0.20 0.00

Iani Chaos region
04_FRT_134D2
(-28°C; 7.5 mbar)

Antoniadi crater
03_FRT_9312
(-43°C; 5.9 mbar)

Antoniadi crater
02_FRT_9BCE
(-28°C; 6.0 mbar)

Camichel crater
01_HRL_985E
(-36°C; 5.8 mbar)

H_2O ice
Mars North Polar Cap
FRT_17669

Simulated reflectance

0.10 0.08 0.06 0.10 0.09 0.08

Opal-CT
1551 sample (-35.8°C)

Opal-A
785 sample (-36.4°C)

Reflectance

0.80 0.60 0.40 0.20

Montmorillonite
SZa-1 (USGS; ambient)

8000 7500 7000 6500 6000 5500 5000 4500 4000

Wavenumber (cm^{-1})